Geochimica et Cosmochimica Acta
December 2015, Volume 171, Pages 61-79
http://dx.doi.org/10.1016/j.gca.2015.08.021
http://archimer.ifremer.fr/doc/00278/38965/
© Published by Elsevier Ltd.

Achimer
http://archimer.ifremer.fr

Iron mineral structure, reactivity, and isotopic composition in a South Pacific Gyre ferromanganese nodule over 4 Ma

Marcus Matthew A. [1, *], Edwards Katrina J. [2], Gueguen Bleuenn [3, 4, 5], Fakra Sirine C. [1], Horn Gregory [2], Jelinski Nicolas A. [6], Rouxel Olivier [3], Sorensen Jeffry [6], Toner Brandy M. [6]

[1] Advanced Light Source, Lawrence Berkeley National Laboratory, Berkeley CA 94720, USA
[2] Department of Biological Sciences, University of Southern California, Los Angeles, CA, USA
[3] IFREMER, Centre de Brest, Unité Géosciences Marines, 29280 Plouzané, France
[4] Institut Universitaire Européen de la Mer, UMR 6538, Université de Brest, BP 80 F- 29280 Plouzané, France
[5] Department of Geology and Geophysics, Yale University, New Haven, CT, USA 06511
[6] Department of Soil, Water, and Climate, University of Minnesota, St. Paul, MN, USA 55108

* Corresponding author : Matthew A. Marcus, Tel.: 510 495 2106; fax: 510 486 4102 ;
email address : mamarcus@lbl.gov

Abstract :

Deep-sea ferromanganese nodules accumulate trace elements from seawater and underlying sediment porewaters during the growth of concentric mineral layers over millions of years. These trace elements have the potential to record past ocean geochemical conditions. The goal of this study was to determine whether Fe mineral alteration occurs and how the speciation of trace elements responds to alteration over ~3.7 Ma of marine ferromanganese nodule (MFN) formation, a timeline constrained by estimates from 9Be/10Be concentrations in the nodule material. We determined Fe-bearing phases and Fe isotope composition in a South Pacific Gyre (SPG) nodule. Specifically, the distribution patterns and speciation of trace element uptake by these Fe phases were investigated. The time interval covered by the growth of our sample of the nodule was derived from 9Be/10Be accelerator mass spectrometry (AMS). The composition and distribution of major and trace elements were mapped at various spatial scales, using micro-X-ray fluorescence (μXRF), electron microprobe analysis (EMPA), and inductively coupled plasma mass spectrometry (ICP-MS). Fe phases were characterized by micro-extended X-ray absorption fine structure (μEXAFS) spectroscopy and micro-X-ray diffraction (μXRD). Speciation of Ti and V, associated with Fe, was measured using micro-X-ray absorption near edge structure (μXANES) spectroscopy. Iron isotope composition (δ56/54Fe) in subsamples of 1-3 mm increments along the radius of the nodule was determined with multiple-collector ICP-MS (MC-ICP-MS). The SPG nodule formed through primarily hydrogeneous inputs at a rate of 4.0 ± 0.4 mm/Ma. The nodule exhibited a high diversity of Fe mineral phases: feroxyhite (δ-FeOOH), goethite (α-FeOOH), lepidocrocite (γ-FeOOH), and poorly ordered ferrihydrite-like phases. These findings provide evidence that Fe oxyhydroxides within the nodule undergo alteration to more stable phases over millions of years. Trace Ti and V were spatially correlated with Fe and found to be adsorbed to Fe-bearing minerals. Ti/Fe and V/Fe ratios, and Ti and V speciation, did not vary along the nodule radius. The δ56/54Fe values, when averaged over sample increments representing 0.25 to 0.75 Ma, were homogeneous within uncertainty along the nodule radius, at -0.12 ± 0.07 ‰ (2sd, n=10). Our results indicate that the Fe isotope composition of the

Please note that this is an author-produced PDF of an article accepted for publication following peer review. The definitive publisher-authenticated version is available on the publisher Web site.

nodule remained constant during nodule growth and that mineral alteration did not affect the primary Fe isotope composition of the nodule. Furthermore, the average δ56/54Fe value of -0.12 ‰ we find is consistent with Fe sourced from continental eolian particles (dust). Despite mineral alteration, the trace element partitioning of Ti and V, and Fe isotope composition, do not appear to change within the sensitivity of our measurements. These findings suggest that Fe oxyhydroxides within hydrogenetic ferromanganese nodules are out of geochemical contact with seawater once they are covered by subsequent concentric mineral layers. Even though Fe-bearing minerals are altered, trace element ratios, speciation and Fe isotope composition are preserved within the nodule.

Please note that this is an author-produced PDF of an article accepted for publication following peer review. The definitive publisher-authenticated version is available on the publisher Web site.

ACCEPTED MANUSCRIPT

1. INTRODUCTION

Marine ferromanganese nodules (MFN) have attracted interest for many decades due to their economic potential and their possible use as recorders of the marine geochemical environment over millions of years (Calvert and Cronan, 1978; Koschinsky and Hein, 2003). These nodules are among the slowest-growing natural materials known, with growth rates measured in mm/Ma, and characterized by alternating layers of Mn-rich and Fe-rich phases precipitated around a nucleus (e.g. shark tooth, rock debris) (Banerjee et al., 1999; de Lange et al., 1992). MFNs occur on the seafloor in water depths > 4000 m, usually below the calcite compensation depth and in well oxygenated environments. They generally form in inactive tectonic settings where very slow rates of sedimentation (<10 cm/1000 yrs) protect metals from dilution with background sediments. The abyssal plains, such as the Clarion/Clipperton zone in the Central Pacific Ocean have the most abundant nodule fields at the seafloor (Hein et al., 2013). MFNs are different from ferromanganese crusts that are deposited in shallower environments mostly on the flanks of seamounts by hydrogenous precipitation from dissolved trace metals in seawater. The sources of metals to MFNs can include: (1) a hydrogenetic source, (2) a diagenetic source, largely derived from the decay of organic matter, and (3) a hydrothermal source. The diagenetic source is generally considered predominant, indicating the important role of organic matter decay during early diagenesis processes in oxic sediments that release dissolved trace metals to sediment porewaters (Heggie et al., 1986; Klinkhammer et al., 1982; Morford and Emerson, 1999; Sawlan and Murray, 1983). However, hydrogenetic nodules do form under low-productivity waters. In addition, microorganisms have been proposed as geochemical agents in Mn- and Fe-cycling in sediments leading to the formation of MFN (Wang et al., 2009), whereas sorption experiments of Ni on ferrihydrite showed that the presence of organic material decreased the sorption efficiency of Ni on the mineral (Eickhoff et al., 2014)

Iron is often the most or second-most abundant metal in MFNs, and is present as Fe-bearing mineral phases known to be chemically reactive with trace elements. For instance, rare earth elements in MFN are thought to be hosted by the Fe-phases (Elderfield et al., 1981). Although the properties of Mn minerals and trace elements in MFNs have been examined many times over the past decades (Aplin and Cronan, 1985; Banakar and Tarkian, 1991; Cronan, 1975; Dymond et al., 1984; Elderfield et al., 1981; Martin-Barajas et al., 1991; Verlaan et al., 2004;

ACCEPTED MANUSCRIPT

Yoshikawa, 1991), there has been comparatively little research on Fe mineral phases. This is likely due to analytical difficulties associated with distinguishing among the suite of Fe oxyhydroxide phases that may occur, as well as the fine spatial scale over which mineralogy varies in nodules. The use of traditional techniques such as powder X-ray diffraction (XRD) and ^{57}Fe Mossbauer spectroscopy has been largely unsuccessful due to the poorly crystalline, distorted structures, and intergrowth with Mn oxides (Murad and Schwertmann, 1988). Further, most of the literature on MFN mineralogy is unreliable; for example, it was once typical to identify a Mn-rich phase as "todokorite" based on optical microscopy and perhaps a bulk XRD pattern. Synchrotron X-ray microprobe (μXRF, μXAS and μXRD) techniques allow us to tackle these issues on unprocessed samples (Manceau et al., 2002). To date, this approach has been used infrequently, but successfully, to study the incorporation of trace elements in nodule nanophase oxides and using marine ferromanganese deposits as natural long-term sorption laboratories (Manceau et al., 2014; Marcus et al., 2004b; Takahashi et al., 2007; Takahashi et al., 2000).

Despite the analytical challenges, the structure and reactivity of Fe minerals in MFNs must be defined if we wish to validate them as recorders of past marine conditions. Specifically, mineral transformation processes may result in a blurring or over-writing of trace element speciation and isotopic signatures. For example, it is known that trace metal associations (e.g. Ni, Zn) with Fe minerals (e.g. goethite) can change in the presence of Fe^{2+} under laboratory conditions, especially under advective flow conditions (Frierdich and Catalano, 2012; Frierdich et al., 2011). Ferrihydrite in particular has been shown to incorporate additional Cu and Zn during Fe^{2+} catalyzed recrystallization, as reviewed by Latta et al. (2012). From a Mn mineral perspective, it has been demonstrated in laboratory studies that Ni uptake by the Mn oxide birnessite is pH dependent, but also reversible, calling into question its use as a paleo-pH indicator (Peacock, 2009). However, transition metals such as Ni, Mn, and Co have been shown to slow the rate of recrystallization of poorly ordered Fe oxyhydroxides (Cornell et al., 1992); which could result in preservation of the original chemical association between the mineral and trace element. Perhaps the primary factor in preservation of trace element signatures is the degree to which buried mineral layers are in geochemical contact with younger deposits and current seawater conditions. If recrystallization creates Fe mineral phases with similar reactive properties and the mineral is out of contact with seawater, then we might expect the preservation of trace element signatures over time in nodules.

In the present contribution, we use a variety of spectroscopic and isotopic approaches to address whether Fe minerals transform to stable phases in a South Pacific Gyre over time. In

ACCEPTED MANUSCRIPT

addition, we ask whether Fe minerals can retain the geochemical signatures of associated trace elements and faithfully record the Fe isotope composition of seawater through time.

2. Nodule description and methods

2.1 Description of the sample

2.1.1 Sample collection and handling

The nodule was collected December 24, 2006 (D'Hondt et al., 2009), at 26°03.09'S, 156°53.65'W, at 5126 m water depth during the Knox02RR cruise of the RV Roger Revelle, using a multicore sampler. The site, South Pacific Gyre-2 (SPG-2), is characterized as follows: SPG-2 is located in a region of abyssal hill topography trending roughly NE-SW (065°). Two populations of abyssal hill topography are present. The larger hills have relief ranging from 300-400 m with a spacing of ~ 20 km. The smaller hills are superimposed on the larger abyssal hills and have a relief of about 50-100 m and a spacing of about 5-6 km. Several small seamounts (2 km-wide, 300 m-high) are scattered about the region. The largest seamount is located ~3-4 km south of the coring site.

The coring site is located within magnetic polarity Chron 34n so the crustal age may range from 84 - 124.6 Ma (Gradstein and Ogg, 2002). Based on a tectonic reconstruction of the region (Larson et al., 2002), the crust was accreted along the Pacific-Phoenix spreading center ~95 Ma ago at ultra-fast spreading rates (~90 km/Ma, half-rate). The sediment on which the nodule rested (half-buried) was homogeneous dark brown clay with micronodules and no microfossils seen on a smear slide. The nodule described in this study was approximately spherical (diameter was 65 – 68 mm as obtained from nine measurements along three axes) and was observed shipboard to be partially buried in sediment at the top of the sediment core. However, the actual orientation of the nodule at the seafloor is not known. The sample was collected as part of a much larger effort to document the nature of life in slowly-accumulating sediments of low primary productivity and great age.

A polished petrographic thin section of the nodule was prepared by Spectrum Petrographics, Inc. The nodule was embedded in 3M Scotchcast #3, mounted on a fused silica slide with Loctite Impruv 363 adhesive, and sectioned to a 30 µm slice and diamond-polished to an electron-microprobe finish. In addition, 1mm-thick sections were made and cut into 2mm-wide "matchsticks" for X-ray tomography, wet-chemical analysis and µXRD.

ACCEPTED MANUSCRIPT

159 *2.1.2 Chemical composition*

160 The "matchstick" nodule sample was sectioned length-wise into 10 sub-samples using a
161 microdrill device (Micromill®). Each fraction was dissolved in a mixture of 6 mL concentrated
162 HNO_3 (sub-boiled) and 2 mL concentrated HF (Trace metal or Optima grade) to ensure complete
163 dissolution of silicate phases. Solutions were evaporated on hot plates at 80°C. Dry residues were
164 then dissolved in 5 mL concentrated HNO_3 and 5 mL 6 M HCl and evaporated to dryness at
165 80°C. This last step was repeated once to ensure completed dissolution of non-siliceous materials
166 including fluorides that could have formed during the first digestion step. Archive solutions were
167 kept in 5 mL 6M HCl. Elemental concentrations were measured on an ICP-AES (Inductively
168 Coupled Plasma Atomic Emission Spectroscopy) instrument, HORIBA Jobin YVON, ULTIMA
169 2) operated by Pôle-Spectrométrie-Océan (PSO, Ifremer/IUEM, Brest, France). Calibration of the
170 concentrations during analysis was done using a multi-elemental solution. As a consistency
171 check, two geostandards of nodule samples (USGS Nod P1 and USGS Nod A1) were analyzed
172 alongside our samples. The results, shown at the bottom of Table 1, are consistent with published
173 data (Axelsson et al., 2002).
174 Due to the process involved in micro-drilling and ICP-AES analysis, and potential dilution by
175 embedding resin, the nodule material could not be accurately weighed, but about 10 mg was
176 collected for each subsample. Therefore, for consistency and comparison with electron
177 microprobe geochemical data, we did not report ICP-AES data in microgram of element per gram
178 of rock as it is the common usage in geochemistry, but instead data were normalized to Fe and
179 expressed in grams of element per gram of Fe. We defined two different zones in the nodule, the
180 "inner" and the "outer" nodule zones. The "outer" zone corresponds to the most external layers
181 including the surface directly in contact with ambient seawater. Therefore, the "inner" zone is
182 also the oldest and the "outer" zone is the youngest zone of the nodule. These zones are
183 morphologically distinct, as shown in Figures 1 and 3 and discussed below. Note that our section
184 of the nodule does not include the part in contact with the nucleus.
185 The fine-scale elemental composition and mineral textures was examined with electron
186 microprobe analysis using a JEOL JXA-8900 Electron Probe Microanalyzer and wavelength-
187 dispersive spectrometer at the Electron Microprobe Laboratory, Earth Science Department,
188 University of Minnesota.
189

190 **2.2 Nodule material relative age estimates and apparent growth rate**

191 *2.2.1* ***$^{9}Be/^{10}Be$ systematics***

ACCEPTED MANUSCRIPT

Most relative age estimates and apparent growth rates of Fe-Mn nodules have been constrained by relying on the unique characteristics of the $^{9}Be/^{10}Be$ system in oceanic environments (Graham et al., 2004). The delivery of ^{9}Be (the stable Be isotope) and ^{10}Be (a long-lived radioisotope of Be with a half-life of ~ 1.38 Mya) to well-mixed deep ocean waters and their subsequent incorporation into growing Fe-Mn nodules can be used as a proxy for the relative ages of nodule sections when differences in the concentration of ^{10}Be or $^{9}Be/^{10}Be$ ratio with depth in the nodule are known (Graham et al., 2004; Segl et al., 1989). Although many processes contribute to the ultimate concentrations and ratios of ^{9}Be and ^{10}Be in ocean waters, two important general principles apply: 1) the delivery of ^{9}Be to oceans is primarily from terrestrial sediments and is thus (at least outside of sediment plumes at continental shelves) influenced by globally averaged erosion rates, and 2) the delivery of 10Be to oceans is primarily due to direct deposition after cosmogenic production in the upper atmosphere (due to spallation reactions involving high-energy cosmic particles and gaseous O and N atoms) and is therefore dependent on the long-term variation of solar activity (Willenbring and von Blanckenburg, 2010d) Both of these factors are known to vary over time, however ratios appear to vary around a long-term mean (Willenbring and von Blanckenburg, 2010a) and growth rate estimates from ^{10}Be remain the major tool available to constrain and assess differences in ferromanganese nodule growth behavior due to environmental factors.

2.2.2 Chemical extraction and determination of ^{9}Be and ^{10}Be concentrations

^{9}Be and ^{10}Be concentrations were determined in two increments between 0-5 mm and 15-20 mm (as measured from the nodule core) from the nodule cross-section ("inner" and "outer", respectively). Material from these increments was extracted in three parallel sections - the middle material was used for ^{10}Be determination and the two outer sections used for ^{9}Be determination.

^{9}Be was determined by digesting approximately 0.25g of ground nodule material in 6M HCl for 3 hrs at 110 ^{o}C. Samples were analyzed in a Thermo Scientific XSERIES 2 ICP-MS with ESI PC3 Peltier cooled spray chamber, SC-FAST injection loop, and SC-4 autosampler (Aqueous Geochemistry Laboratory, Earth Science Department, University of Minnesota). Samples were diluted 20× and 20 ppb of Y internal standard was added. ^{10}Be was extracted from the nodule material through a series of acidification steps and cation column chromatography prior to being oxidized and analyzed by AMS. The methodology used here is modified from Ebert et al. (2012). Approximately 0.25 g of ground nodule material was digested in Teflon vessels with 6 M HCl and 250 µg of spiked ^{9}Be carrier at 110 ^{o}C for 3 hr. 4ml of HF was added to the cation solution in

ACCEPTED MANUSCRIPT

two steps to bind excess Ca and Mg. After each HF addition step, 2 mL of ultrapure H_2O_2 was added to remove organics. The ultrapure water containing Be and other cations was removed from the fluoride cake via centrifugation and pipetting. Ion exchange chromatography (both anion and cation removal steps) was used to purify Be cations from the bulk cation solution. Be-hydroxides were precipitated from the purified cation solution by titration to pH 9 through the addition of ammonium hydroxide. The supernatant was decanted and the precipitate was washed several times with ultrapure water and dried overnight at 100 ^{o}C in low-boron quartz vials. The dry precipitate was flame-oxidized at > 850 ^{o}C to form BeO powder and pressed into cathodes for AMS analysis at PRIME Lab, Purdue University, USA.

2.2.3 Growth Rate Estimation

Nodule growth rate was estimated by the ^{10}Be dating method developed for ferromanganese nodule segments ((Baturin and Savenko, 1989; Graham et al., 2004; Somayajulu, 2000). This dating method is based on the relative difference in isotopic composition of two layers (Graham et al., 2004):

$$\text{Age difference} = (t_{1/2}/\ln(2))\ln(I/O)$$

where $t_{1/2}$ is the half-life of ^{10}Be, and I and O are the isotopic composition of the "inner" and "outer" increments, respectively. The average growth rate between segments can then be determined by dividing the age difference by the distance across the nodule cross-section measured between segment centroids. Several previous growth rates reported for ferromanganese nodules used the older half-life estimate for ^{10}Be of 1.5 +/- 0.1 Ma.(Bhat et al., 1973). Here, we report absolute growth rate estimates using the revised consensus half-life for ^{10}Be (Chmeleff et al., 2010; Korschinek et al., 2010) of 1.387 Ma and also report apparent growth rate estimates using the former value of 1.5 Ma to facilitate direct comparison with previous work (i.e. Graham et al., 2004). The major assumptions of this equation is that the layers concerned had the same initial isotopic concentration when they were formed, and that there has been no isotopic exchange or fractionation since that time.

Some authors have applied the isotopic ratio of ^{10}Be/^{9}Be of the segments, instead of bulk ^{10}Be concentrations (atoms g^{-1}) to calculate age differences as there is evidence that the ^{10}Be/^{9}Be ratio of seawater is more invariant over time than the absolute ^{10}Be concentration (Graham et al., 2004; Segl et al., 1989). _ENREF_90Therefore, we report age differences and growth rates here from based on both the Be isotopic ratio and absolute ^{10}Be concentrations.

ACCEPTED MANUSCRIPT

260

261 **2.3 µXRF, µXAS, and µXRD**

262 In order to study the morphology and element distributions in more detail micro X-ray
263 fluorescence (µXRF) maps were acquired at Beamline 10.3.2 of the Advanced Light Source
264 (Marcus et al., 2004a). For a general survey, a long map was acquired over a strip 20 mm long by
265 1mm wide, with 20 µm pixels. All µXRF maps on the nodule were acquired at 10 keV, using
266 dwell times of 30-50 ms and pixel sizes of 5-10 µm. Fluorescence emission signals for Fe, Mn,
267 Ni, Cu, Zn, Ti, Ca, and additionally in some areas Ce, V, P and Co were recorded with a seven-
268 element Ge solid state fluorescence detector (Canberra).

269 Micro-X-ray absorption spectra (µXAS) at the Fe, V and Ti K-edges were recorded in
270 fluorescence mode on selected spots of the µXRF maps. The energy was calibrated with respect
271 to the respective metal foils, whose inflection-point energy were taken to be 7110.75 (Fe),
272 5463.76 (V) and 4966.40 eV (Ti) respectively. Data were calibrated, deadtime-corrected, pre-
273 edge subtracted and post-edge normalized using custom LabVIEW programs available at the
274 beamline (https://sites.google.com/a/lbl.gov/microxas-lbl-gov/software). The data range for
275 micro X-ray absorption near edge structure (µXANES) spectroscopy was 100 eV below up to
276 300 eV above the edge, while micro extended X-ray absorption fine structure (µEXAFS)
277 spectroscopy data were taken up to 500 eV above the edge. Fe µXANES spectra were fit by
278 least-square linear combination (LCF) to a large Fe database (Marcus et al., 2008). Over-
279 absorption is significant in the more Fe-rich spots, and is taken as a free parameter in a simple
280 model (planar, thick sample). Since the cited paper was published, a number of new spectra
281 were added, including one for feroxyhite, a potentially-important species for nodules. This
282 sample was prepared by the method of Schwertmann and Cornell (2000) and verified by powder
283 XRD at the Characterization Facility, University of Minnesota, using a Siemens D-500
284 diffractometer with cobalt source. The observed [Si]/[Fe] ratios in the nodule are low enough to
285 rule out the presence of a significant (>10%) amount of clays or most other silicates, so these
286 were omitted from the set of fitting references. For V and Ti, our libraries are much more
287 limited. For Ti, the only standard we had whose XANES was at all similar to that of the sample
288 was ilmenite. For V, we used samples of V(V) sorbed on δ-MnO_2 and ferrihydrite. Hexagonal
289 birnessite ($K_{0.5}Mn_2O_4 \cdot 1.5H_2O$) was synthesized by published methods (McKenzie, 1971;
290 Villalobos et al., 2003) using purified water (18.2 MΩ; MilliQ) and ACS grade reagents. Briefly,
291 hexagonal birnessite was prepared by boiling a 2.5 L solution of 0.4 mol/L $KMnO_4$ with vigorous
292 mechanical stirring. The precipitate was formed through drop wise addition of 163 mL of

ACCEPTED MANUSCRIPT

concentrated HCl using a burette. V adsorption experiments were performed using goethite and 2-line ferrihydrite, synthesized by standard procedures (Schwertman and Cornell, 1991).

The precipitates were washed in 3 centrifuge-resuspend cycles with purified water, separated from suspension using vacuum filtration (0.22 µm Millipore polyethersulfone), and then freeze dried and stored as a dry power.

Fe micro-EXAFS spectra were analyzed with $k^3\chi(k)$ weighting, out to $k = 11 Å^{-1}$. For those spectra in which over-absorption was significant, we performed LCF of the XANES spectra to estimate the amount of over-absorption, applied that correction to the post-edge normalized spectra, and extracted the EXAFS signal from these corrected spectra. EXAFS data were then fitted using either linear combinations of reference EXAFS spectra or by shell-by-shell fitting using Artemis (Newville, 2001; Ravel and Newville, 2005). For the latter, the structures of goethite and lepidocrocite were used to create FEFF6l input files from which to extract Fe-O and Fe-Fe paths out to 3.5.Å, which encompasses face, edge, and corner-sharing FeO_6 octahedra. This analysis is similar to the polyhedron-centered analysis which was done for poorly-ordered biogenic Fe oxide (Toner et al., 2009). For some of the spectra, we used a shell-by-shell fitting approach based on experimental amplitudes and phases (feroxyhite and lepidocrocite, for Fe-O and Fe-Fe paths), which gave results consistent with the Artemis fitting.

Micro XRD patterns were recorded with a Bruker SMART6000 CCD at 17keV (λ = 0.7293 Å) and 240 s acquisition time. The patterns were radially-integrated and calibrated using alumina powder and fit2D software (Hammersley, 1997). Micro XRD patterns were recorded at the µXAS spot locations on the thin sections, and on a nearby blank spot on the silica substrate so as to background subtract the data. In order to improve the sensitivity of the XRD, we also mounted a thick section ("matchstick") in such a way that the beam passed through ~1 mm of sample without striking the substrate.

2.4 Fe isotope analyses

Iron isotope compositions were analyzed on a multi collector (MC-) ICP-MS (Inductively-Coupled-Plasma Mass-Spectrometer) (Neptune, Thermo-Scientific) at Pôle-Spectrométrie-Océan (PSO, Ifremer/IUEM, Brest, France) on the 10 subsamples of the nodule analyzed for the bulk geochemistry (see section 2.1.2). After chemical separation of Fe from the matrix through chromatography columns filled with an anion-exchange resin AG1-X8, $^{56}Fe/^{54}Fe$ and $^{57}Fe/^{54}Fe$ isotope ratios were measured using a nickel-doping method to correct samples for

ACCEPTED MANUSCRIPT

instrumental mass discrimination combined with a standard-sample-bracketing method (Albarède and Beard, 2004; Rouxel et al., 2008; Rouxel et al., 2005) This analysis scheme allows us to determine a two standard deviation of 0.07-0.09 ‰ based on replicate measurements of IRMM-14 isotopic standard. $^{56}Fe/^{54}Fe$ isotope ratios of samples are reported relative to IRMM-14 Reference Material according to the conventional delta notation (1) used for stable isotope systematics.

$$\delta^{56/54}\mathrm{Fe} = [(^{56}\mathrm{Fe}/^{54}\mathrm{Fe}_{\mathrm{sample}}) / (^{56}\mathrm{Fe}/^{54}\mathrm{Fe}_{\mathrm{IRMM\text{-}14}}) - 1] \times 1000 \quad (1)$$

The relationships between $\delta^{56/54}Fe$ and $\delta^{57/54}Fe$ of the samples analyzed in this work plot on a single mass fractionation line and only $\delta^{56/54}Fe$ values are discussed in this paper.

The iron isotope composition of the USGS geological reference material nodule (Nod-A-1), yielding $\delta^{56/54}Fe = -0.37 \pm 0.06$ (2sd, n=12) is consistent with previously published data (Dideriksen et al., 2006). We also determined the long-term average value of Nod-P-1 USGS geological reference material and obtained $\delta^{56/54}Fe = -0.51 \pm 0.09$ (2sd, n=11). Results for Nod-A-1 and Nod-P-1 reported in Table 1 correspond the $\delta^{56/54}Fe$ values obtained within the same analytical conditions than for the nodule samples obtained after micro-drilling.

3. Results

3.1 Nodule growth rate

The chronometer we used was based on two Be isotopes. ^{9}Be and ^{10}Be. ^{10}Be is a radioactive nuclide produced in the atmosphere (cosmogenic nuclide). The production rate of ^{10}Be in the atmosphere is presumably constant and when this flux reaches the oceans through aerosol rainfall, it mixes with ^{9}Be present in the oceans after riverine inputs. The seawater isotope ratio of $^{10}Be/^{9}Be$ has remained constant in modern oceans (Willenbring and von Blanckenburg, 2010a, d), and therefore when nodules precipitate from seawater they incorporate Be which has the same $^{10}Be/^{9}Be$ ratio as ambient seawater. ^{10}Be decays with a half of 1.39 Ma (Chmeleff et al., 2010), therefore as the nodule grows, $^{10}Be/^{9}Be$ ratios in the older layers of the nodule will decrease and using the exponential law of radioactive decay we can reconstruct an age model for the different layers in the nodule.

The ^{9}Be and ^{10}Be values for the nodule are displayed in **Table EA1**. Both ^{9}Be and ^{10}Be concentrations for this nodule (3.6-3.8 mg/kg and 0.54 – 3.41 x 10^{9} atoms g^{-1}, respectively) fall within the range of concentrations reported in previous publications (Segl et al. 1989; Graham et al. 2004). The growth rates estimated for this nodule (from 3.8 ± 0.7 to 4.2 ± 0.7 mm/Ma) using

ACCEPTED MANUSCRIPT

multiple estimation methods appear to be slightly lower than the range of rates reported in Graham et al. 2004 (4.7 - 32 mm/Ma), but are well within the range of globally compiled estimates (1.24 - 5.17 mm/Ma) from Willenbring and von Blanckenburg (2010a).

3.2 Chemical composition

The chemical composition of the South Pacific Gyre-2 (SPG-2) nodule, as determined by analyses of 10 increments spanning the 19.5 mm radius of the nodule in 1 to 3 mm lengths, is displayed in **Table 1**. All elemental concentrations are normalized by Fe. In addition to the bulk average of the 1 to 3 mm increments, Electron Microprobe Analyzer (EMPA) was used to measure fine-scale elemental composition in three transects displayed in **Figure 1**. The EMPA data are expressed in wt %, but note that the sum of the weights does not equal 100% because the nodule is porous, rich in hydrous mineral phases, and CO_2 (**Tables EA2, EA3**).

Figure 2 shows a ternary plot of Mn, Fe and (Ni + Co) × 10 and displays the properties distinguishing among hydrothermal, hydrogenetic, and diagenetic sourced marine Fe/Mn-rich deposits. The three numbers represented by a point in this plot are $X_{\mathrm{Fe}} = [\mathrm{Fe}]/([\mathrm{Fe}]+[\mathrm{Mn}]+([\mathrm{Ni}]+[\mathrm{Co}])\times 10)$, $X_{\mathrm{Mn}} = [\mathrm{Mn}]/([\mathrm{Fe}]+[\mathrm{Mn}]+([\mathrm{Ni}]+[\mathrm{Co}])\times 10)$, and $X_{\mathrm{NiCo}} = ([\mathrm{Ni}]+[\mathrm{Co}])\times 10/([\mathrm{Fe}]+[\mathrm{Mn}]+([\mathrm{Ni}]+[\mathrm{Co}])\times 10))$, with [..] representing atomic percentages. The left-hand corner represents X_{Fe}=1, the right-hand corner X_{Mn}=1, and the top X_{NiCo}=1, which implies that X_{Fe}+ X_{Mn}=0.9. Note that this representation works even using data normalized by [Fe]. Three types of data were compared: (1) the EMPA data for "inner" and "outer" transects (as defined in **Figure 1b, c**); (2) the bulk average ICP-AES data for the 1 to 3 mm increments; and (3) selected literature data for the North and South Pacific Ocean (Halbach et al., 1981). Oceanic metalliferous deposits that have a high diagenetic component plot in the "diagenetic field" of the ternary diagram of Figure 2 (i.e. high Mn content and a trend towards higher Ni+Co), deposits that have a hydrothermal contribution have generally low Ni+Co contents but variable Mn and Fe contents ("hydrothermal field"), and finally the "hydrogenetic field" contains deposits formed from seawater and they are characterized by high Ni+Co and the proportions of Mn and Fe in these deposits are relatively similar. Northern Pacific nodules generally have a diagenetic contribution, as shown by the trend towards higher Mn/Fe and (Ni+Co)/Fe, whereas the SPG-2 nodule displays a trend toward a hydrogenetic contribution (lower Mn/Fe and (Ni+Co)/Fe content). Together with reference datasets, the SPG-2 composition indicates that it was primarily a hydrogenetic deposit throughout its growth history. This finding is consistent with the documented low flux of organic matter to the seafloor of the

ACCEPTED MANUSCRIPT

South Pacific Gyre (Jahnke, 1996) and reduced diagenetic contributions to the growth of the SPG-2 nodule.

3.3 Nodule morphology and trace element distributions

Backscatter scanning electron microscopy and electron microprobe analyses revealed morphological differences between "inner" and "outer" zones of the nodule (**Figure 1**, **2**). In both zones, concretions with layered growth habits of two basic forms were observed: a "botryoidal" morphology of concentric, layered mineral growth and a porous "matrix" material between the botryoids. These growth habits have been previously reported (Halbach et al., 1981).

A tricolor μXRF map showing the distributions of Fe, Mn and Ni from the "outer" to "inner" zone is displayed in **Figure 3** along with a photomicrograph and the fluorescence counts for Fe, Mn and Ni along the nodule radius. A clear transition in the elemental composition was observed at approximately 12 mm: Fe increased and Mn decreased along the transect toward the nodule center. These results are consistent with the EMPA Mn/Fe data (**Table EA3**) but not with the bulk average ICP-AES data for the 1 to 3 mm increments. Bulk ICP-AES analyses of the 10 subsamples of the nodule do not show significant variations in metal/Fe (**Table 1**) across the nodule transect, suggesting uniform metal/Fe ratios in Fe and Mn-rich phases at the scale of sampling intervals (1 to 3 mm). Bulk ICP-AES analyses suggest the geochemical composition of the nodule is homogenous at the bulk (1-3 mm) scale, while μXRF and EMPA data reveal a fine-scale geochemical variability along the nodule, not captured by millimeter-scale analyses.

Some trace elements, notably Ti, V and, to a lesser extent, Zn, are associated with Fe in the nodule (EMPA data; **Figure 4**; V shown in **Figure 5**.). Micro-XRF maps of the "inner" and "outer" zones, displayed in **Figure 5**, also show this pattern. For Ti and V, the correlation with Fe is good, as viewed in red-blue bicolor maps of Fe+Ti (correlation coefficient 0.78 for "inner" and 0.92 for "outer") and Fe+V (correlation coefficient 0.86 for inner and 0.85 for outer) (**Figure 6**), in which the hue is nearly uniform. Note that the Fe+Ti correlation for "inner" came from the same XRF map as the Fe+V correlation for "inner", so cover the same number of independent pixels. The same is true for the Fe+Ti and Fe+V correlations in "outer". Since these numbers derive from pixel-by-pixel scatterplots, it is difficult to define the number of statistically-independent points since the samples have features which are much bigger than a pixel. When Fe is shown as blue and Ti or V in red, the matrix shows slightly bluer than the "botryoids", indicating a slightly lower (V,Ti)/Fe ratio in the matrix than elsewhere. For Ti, the difference in ratio is about 20%, while the two types of material differ in V/Fe ratio by only 6%. The inverse correlation between Ti/Fe and Mn/Fe ratios (**Figure 4d**) in the "inner" zone indicates that Ti is

ACCEPTED MANUSCRIPT

mostly associated with Fe. The distribution of Zn also has some features in common with that of Fe, in particular, an enrichment in the "matrix" areas (**Figure 5**). These patterns of distribution are consistent with Ti and V bound to or incorporated in Fe-bearing mineral phases in the "botryoids", and Zn bound to or incorporated in Fe-bearing mineral phases in the "matrix".

Clear correlations in Ni/Fe and Co/Fe ratios versus Mn/Fe suggest that Ni and Co are hosted primarily by Mn-rich minerals (**Figure 4a, b**). The scatter in the Zn/Fe versus Mn/Fe data indicates that Zn may be associated with both Mn and Fe mineral phases (**Figure 4c**). The μXRF data in **Figure 5** corroborate this finding by showing spatial correlation of Zn with both Fe- and Mn-rich features.

From a morphological perspective, the "botryoidal" features are much more pronounced in the "outer" zone of the nodule than in the "inner" zone (e.g. **Figure 5**). In contrast, the Fe-rich "matrix" found in between the "botryoidal" microstructures is a more prominent morphology in the "inner" zone. These growth patterns, as well as the elemental composition, along the radius of the SPG-2 nodule form the basis for our definition of "outer" and "inner" zones having dominant "botryoidal" and "matrix" morphologies.

3.4 Fe-bearing phases

3.4.1 Matrix features

The EXAFS data (Fourier transform) and fits are shown in **Figure 7** along with XRF maps indicating the locations at which the spectra were taken. The data did not differ substantially among various locations within a given zone.

The Fourier transform in **Figure 7b** shows the data for the "inner" zone locations over-plotted with a linear-combination fit using 39% feroxyhite (δ-FeOOH) and 53% goethite (α-FeOOH). Although this fit is a good match to the data, it does not rule out the presence of a few percent of other species. The phase of higher-shell peaks agrees with those in the fit out to 6 Å, presumably due to the long-range order of crystalline goethite. While μXRD was not done on these specific spots, patterns taken at other matrix spots confirm the presence of goethite.

The "matrix" in the "outer" zone is typified by the spectrum and fit shown in **Figure 7a**. This spectrum fits well to 28% lepidocrocite (γ-FeOOH), 39% disordered biogenic oxide (Toner et al., 2009), and 18% goethite. Although the reference material we call "biogenic oxide" is indeed biogenic, this reference represents highly-disordered Fe oxyhydroxide from any source, biogenic or not. The XANES also fits to the same three minerals, but in proportions of 46%, 21% and 30%, respectively. However, no diffraction measurements on any spot show the strong basal (020, d= 6.26Å) reflection expected for lepidocrocite (**Figure 8**). We refer to this reflection as

ACCEPTED MANUSCRIPT

"basal" because lepidocrocite has a layered structure consisting of sheets of edge-sharing octahedra, with the conventional *c*-axis as the layering direction. Other lepidocrocite reflections come close enough to those from other phases such as goethite to make their identification uncertain. The basal reflection, however, is one of the strongest and should therefore appear if well-crystalline lepidocrocite were common in our samples.

The feature in the EXAFS spectrum, that seems to point to lepidocrocite is the prominent peak at 2.7 Å (**Figure 7a**), which corresponds to edge-sharing FeO_6 octahedra. The lepidocrocite structure consists of layers of edge-sharing octahedra. The inter-layer spacing gives rise to the basal reflection, which is not found by μXRD in our samples at any spot. Thus, what the EXAFS indicates is that the material has a large fraction of edge-sharing octahedra relative to a ferrihydrite-like phase or goethite. Shell-by shell fitting yields an average Fe-O distance in the first shell of 2.01 ± 0.015 Å, an Fe-Fe shell 3.06 ± 0.03 Å with a coordination number between 2 and 6 (highly uncertain due to correlation with $\Delta\sigma^2$), and a weak third Fe-Fe shell at 3.38 ± 0.04 Å. The coordination number of this shell is extremely uncertain due to correlation with $\Delta\sigma^2$, but the fit is significantly better with this shell included. The Fe-Fe distances correspond nicely to edge- and corner-sharing octahedra. By comparison, the edge-sharing distance in lepidocrocite is 3.067 Å and the corner-sharing distances in goethite are 3.30 Å and 3.47 Å. In addition, shells at apparent distances of ~3.6 Å and 4.6 Å match those experimentally found for lepidocrocite, and correspond to Fe-Fe distances within the layers. The EXAFS evidence, and apparent lack of the lepidocrocite (002) reflection, is consistent with lepidocrocite nanoparticles that are thin in the *c*-direction but transversely large enough to show the high shells in EXAFS. Note that the biogenic oxide we used as a reference material also has a relatively large ratio of edge-sharing to corner-sharing octahedra, but the overall intensity of that shell is smaller than what we find for the lepidocrocite-like material.

3.4.2 Botryoidal features

The abundance of "botryoidal" material varies between the "inner" and "outer" zones. Principal components analysis (PCA) of Fe EXAFS data from the spots displayed in **Figure 9** reveals a two component system. The spectra can be represented as weighted sums of signals from two materials. The first component is similar to that found for the "inner" matrix and is a combination of feroxyhite and goethite. The second component does not fit to a sum of our reference spectra. The nature of this component is explored below.

Spots 5 and 1 from the "inner" zone (**Figure 9b**) are the best examples of the "botryoidal" Fe material. The Fourier transformed EXAFS signal for Spot 5 are shown in **Figure**

ACCEPTED MANUSCRIPT

10. There are strong peaks at distances similar to those found for corner- and edge-sharing octahedra. The best fit for this spectrum contains four contributions. One is an Fe-O shell represented as the Fe-O first neighbor from feroxyhite. While the Fe-O shell is actually split, the data do not cover a long enough *k*-range to resolve this splitting, and the first shells of our models are well-represented as single shells. Next is a Fe-Fe shell at 3.04 ± 0.038Å with a coordination number (CN) of 2.3-9. The distance found for this shell is consistent with edge-sharing octahedra such as those found in lepidocrocite (3.06 Å), whose edge-sharing peak was used as an experimental reference. This contribution requires an additional mean-square relative displacement (MSRD, second moment of the distance distribution) of 0.014-0.047 $Å^2$, beyond that found in lepidocrocite. This is a significant dispersion, which may reflect an unresolved splitting. The large error bars on this number and the CN reflect parameter correlation between the two. It was found necessary to add a contribution from goethite, which was used without any adjustment except for amount and included all shells out to 3.5 Å. The result showed that 10-25% of the Fe in the sample had to be assumed to be in the form of goethite, though it is possible that some of the other oxides would provide an acceptable fit in this role. Note that the coordination numbers quoted above and below for non-goethite Fe-Fe shells is the average over all Fe atoms; they should be divided by "1-(goethite fraction)" to get the Fe-Fe CNs in the 75-90% of the spot 5 material that is not goethite. A fit with only these three contributions always showed a discrepancy in the FT at around 3.3 Å (apparent). While the phase would match, the amplitude did not. To solve this problem, an additional Fe-Fe shell at 3.45 ± .0.04Å (CN 0.25-0.9) was added to the fit. This distance is comparable to the longer corner-sharing distance in goethite (3.47 Å), thus we interpret it as coming from corner-sharing octahedra in the non-goethite fraction. The MSRD of this shell was assumed to be the same as that in the reference lepidocrocite edge-sharing shell, in order to reduce the number of free parameters. To summarize, the three contributions we find to the Fe environment are goethite, edge-sharing octahedra as in lepidocrocite, and a smaller number of corner-sharing octahedra. We were not able to identify the exact minerals containing these coordination polyhedra (except goethite).

The result of fitting is shown in the bottom panel of **Figure 10**, as the FT magnitude and imaginary part of the data compared with the fit, along with the FT magnitudes of the individual components in the top panel of **Figure 10**.

3.5 Valence states of Ti and V

For Ti, three XANES spectra were taken at "matrix" points from within the "outer" zone. Titanium EXAFS was not possible due to the interference of the Ba L_3 edge, about 280 eV above

ACCEPTED MANUSCRIPT

the Ti K-edge. The best match between the data and references was ilmenite ($FeTiO_3$), as shown in **Figure 11**. The match is not perfect; therefore, the Ti phase within the SPG-2 "outer" "matrix" is not literally ilmenite. Rather, the Ti is likely tetravalent and in octahedral coordination to oxygen which share edges with FeO_6 octahedra: as in the ilmenite structure. Since the "matrix" is largely composed of goethite, which consists of edge-sharing Fe-O octahedra, it is plausible that the spectrum could be accounted for by Ti sorbed to or substituted within goethite.

Vanadium XANES spectra for points from the "inner matrix", "inner botryoid", and "outer botryoid" regions were collected. All of these spectra fit with a two-component model generated by Iterative Target Factor Analysis (ITFA). These two component spectra, ITFA0 and ITFA1, are shown in **Figure 12** along with spectra for V(V) sorbed to 2-line ferrihydrite and δ-MnO_2. Note that the pre-edge peak intensity is lower for δ-MnO_2-sorbed V than for ferrihydrite-sorbed V. Although the pre-peak height is often taken as a sign of valence state, both standards are pentavalent, and the difference is presumably due to the differing symmetry of the V site (Tanaka et al., 1987; Wong et al., 1984).

Figure 13 shows a trend in the V speciation as a function of the local Fe/Mn ratio. The use of the logarithm as the abscissa is not meant to imply any theory; it is for plotting convenience only. In order to understand the trend, an analysis of the V spectral end-members was attempted. **Figure 14** displays fits of ITFA-derived end-member spectra to a combination of V-sorbed standards and, for ITFA0, $LaCl_3 \cdot 7H_2O$, which is needed to represent a small amount of La, whose intense white line makes for a sharp peak at 5489 eV. Vanadium-sorbed goethite (two loadings) and hematite standards did not appear in the fits to either ITFA component. Component ITFA0, which is most prominent in Mn-rich regions, is well-represented by a mixture of the two sorbed standards (29% Mn, 66% Fe, 4% La), suggesting that V is hosted by the nanoparticulate oxides which form the bulk of the nodule. However, ITFA1, which is found in Fe-rich regions, does not fit well. The best fit is to V on δ-MnO_2 alone, which seems odd as there is little Mn in the areas in which ITFA1 is most prominent. In addition, the fit quality is not nearly as good as for ITFA0. It is possible to improve the fit by adding such species as VO_2 and V_2O_5, but it is probable that such a combination merely reconstructs the spectrum without representing the true V species. This is a common challenge with database-driven data fitting; the true species is likely something missing from our database. If V were to be co-deposited in or sorbed on Fe oxyhydroxide in octahedral symmetry, it might also have a low pre-peak. Therefore, the ITFA1 species is tentatively assigned to V in octahedral coordination to oxygen and sorbed to Fe oxyhydroxides. It should be noted that an ITFA end-member may easily be a mixture of actual species as the fit proved true in the case of the ITFA0 discussed above.

ACCEPTED MANUSCRIPT

3.6 Fe isotope composition

Iron isotope composition along the nodule section yields a range of values from -0.16 to -0.07 ± 0.09 ‰ (2sd; **Table 1**). The $\delta^{56/54}$Fe values are constant within uncertainty along the nodule radius with an average value of -0.12 ±0.07 ‰ (2sd) for the 10 increments analyzed. This means that constant Fe isotope values, when averaged over 1 to 3 mm increments or approximately 0.25 to 0.74 Ma intervals, were observed over a period of 4 Ma. We observe that Fe in the "inner" part of the nodule is isotopically identical to Fe present in the "outer" part. Although our measurement interval is too coarse to resolve the isotopic signature of Fe-rich "matrix" versus Mn-rich botryoidal structures, our results are consistent with similar isotope values for "matrix" and "botryoids" because there is more "matrix" in the "inner" part and more "botryoids" in the "outer" part of the nodule, yet the isotope values are the same within experimental error. Moreover, the Fe isotopes recorded in the SPG-2 nodule are within the range of Fe isotope compositions reported for slowly precipitated hydrogenetic ferromanganese crusts (~ -1.2 to ~ +1.6 ‰) (Chu et al., 2006; Horner et al., 2015; Levasseur et al., 2004; Zhu et al., 2000) .

4. Discussion

4.1 Mineral structure and stability

Our results indicate that the Fe speciation in the hydrogenetic South Pacific Gyre nodule is considerably more complex than expected and quite different from the uniform amorphous FeOOH "background" component typically discussed in the literature. Iron oxyhydroxides in the SPG-2 nodule are present in a wide variety of forms – goethite (α-FeOOH), goethite polymorphs feroxyhite (δ'-FeOOH) and nano-lepidocrocite (γ-FeOOH), and biogenic-like ferrihydrite. Each of these phases is thought to form under different environmental conditions (pH and Eh, as examples). Therefore, although the SPG-2 nodule formed in a well-oxygenated environment, the diversity of phases observed should reflect either changes in the deep-sea environment at the sediment-water interface or mineral transformation processes over 3.65 to 4.05 Ma of growth (Schwertmann and Cornell, 2000).

The major trend in Fe speciation within the "matrix" material is a positive correlation between the abundance of stable Fe oxyhydroxides (goethite) and age of deposition. Specifically, Fe EXAFS data reveal that goethite is more abundant in the "inner" (older) deposits than in the "outer" (younger) deposits, 53 mol % and 18 mol %, respectively. Therefore, the SPG-2 nodule

ACCEPTED MANUSCRIPT

hosts a series of phases in which the mineral stability of the Fe oxyhydroxides increases with the age of the deposit.

The "outer matrix" consists of goethite < lepidocrocite < biogenic-like ferrihydrite. Approximately 1/3 of the "outer matrix" is a c-disordered lepidocrocite. Lepidocrocite is typically observed in low oxygen environments with Fe^{2+} present, and is meta-stable with respect to goethite (Schwertmann and Cornell, 2000). In general, the "outer matrix" is characterized by poorly-crystalline Fe oxyhydroxide phases consistent with those observed in modern low-temperature, deep-sea deposits where microbial activity is evident (Toner et al., 2012; Toner et al., 2009). However, microbial activity is not a necessary condition for the precipitation of poorly-crystalline phases. For example, strongly sorbing ligands such as P, Si, and As produce Fe(III) precipitates with these characteristics, and transition metal impurities are known to slow recrystallization processes (Cornell et al., 1992). The structural characteristics and abundance of meta-stable phases suggests that the younger nodule deposits precipitated in the presence of: 1) Fe^{2+} (lepidocrocite-like phase), or 2) metals, ligands, or under the influence of biology (biogenic-like ferrihydrite).

The "inner matrix", can be understood as a mixture of two FeOOH polymorphs, feroxyhite and goethite. In the laboratory, feroxyhite is a meta-stable phase generated by very rapid oxidation of Fe^{2+} in alkaline medium (Chukhrov et al., 1977). In the field, feroxyhite is observed in the pore spaces of sediments hosting Fe^{2+}-rich waters (Carlson and Schwertmann, 1980). In poorly drained soils, where ferrihydrite, lepidocrocite, goethite, and feroxyhite are observed within the profile, feroxyhite is associated with the Mn oxide vernadite (Birnie and Paterson, 1991). While the conditions of feroxyhite formation in laboratory and field studies are consistent with one another and with what we know of the SPG-2 nodule – precipitation in pore spaces near Mn-rich phases – there is little consensus in early literature regarding the stability relationship between feroxyhite and goethite. Chukhrov et al. (1977) proposed that feroxyhite is meta-stable with respect to goethite. However, Carlson and Schwertmann (1980) concluded that feroxyhite does not recrystallize to form goethite, but that the two phases form under different conditions, namely fast oxidation of Fe^{2+} (feroxyhite) versus slow precipitation of Fe^{3+}(goethite). More recently, the stability, and transformation time, for pure oxyhydroxides with respect to hematite in the presence of trace Fe^{2+} was established as: ferrihydrite ≤ feroxyhite < lepidocrocite < akaganeite << goethite (Lu et al., 2011). In agreement with Lu et al., when particle size and mineral surface hydration are considered, goethite was most often the stable phase relative to coarse hematite over a wide range of surface area/particle size conditions; however, at high surface area values ferrihydrite can be the stable phase (Navrotsky et al., 2008). These results

ACCEPTED MANUSCRIPT

631 may indicate that feroxyhite precipitated from a sediment source (fast oxidation of Fe^{2+}), while
632 goethite precipitated in contact with ambient seawater (slow precipitation of Fe^{3+}). In this
633 conceptual framework, the presence of feroxyhite would reflect the "diagenetic" source of metals
634 (sediment porewaters), while goethite would be indicative of the "hydrogenetic" source of metals
635 (seawater dissolved trace metals).

636 Iron minerals with a known role for Fe^{2+} (aq) in their formation were observed in both the
637 "inner" and "outer" matrix materials, feroxyhite and lepidocrocite, respectively. Given the
638 overall hydrogenetic character of the nodule and the low biological productivity of the overlying
639 waters, we do not have a good explanation for a source of Fe^{2+} (aq) or the presence of these
640 minerals. While Fe is abundant in this depositional environment, our understanding of the
641 seafloor conditions points to low availability of Fe^{2+} (aq). Two possible explanations for the
642 presence of Fe^{2+} (aq) should be considered. First, the overall hydrogenetic character of the
643 nodule does not rule out all contributions of material from the sediments. Second, even in low
644 productivity waters there may be enough organic material delivered to the seafloor to promote
645 some Fe reduction during the deposition of the "matrix" materials. We must conclude that either
646 a very low supply of Fe^{2+} (aq) is sufficient to influence the mineralogy of these slowly
647 accumulating deposits or that the presence of lepidocrocite and feroxyhite do not indicate an Fe^{2+}
648 (aq) precursor.
649
650 The "botryoidal" material is a combination of crystalline minerals similar to those found
651 in the "matrix", plus another material whose most distinctive feature is the presence of edge-
652 sharing octahedra with considerable dispersion in Fe-Fe distance. In the "botryoidal"
653 microstructures, as opposed to the "matrix", there is considerable Mn in addition to the Fe. Thus,
654 the possibility should be considered that we have a mixed phase in which the nearest cation
655 neighbor to Fe is not always Fe but is sometimes Mn, such as in "Fe-vernadite". However, the
656 "botryoidal" material need not be a single phase, and could include Fe-rich and Mn-rich material
657 too finely intergrown to have been resolved in this study. If the two phases have differing Fe-Fe
658 distances, then the resulting average EXAFS could show a large MSRD. However, because
659 linear-combination fitting did not produce a match, at least one of these phases must be
660 something not found in our spectral database. Consistent with intergrowth between Mn and Fe
661 minerals, the "botryoidal" material includes several percent of other transition metals such as Cu,
662 Ni, Co and Zn, which are known to be associated primarily with Mn oxide minerals in
663 hydrogenetic ferromanganese crusts (Halbach and Puteanus, 1984; Hein et al., 2003; Koschinsky
664 and Halbach, 1995; Koschinsky and Hein, 2003; Koschinsky et al., 1997).

ACCEPTED MANUSCRIPT

4.2 Trace element association with Fe oxyhydroxides

For the SPG-2 nodule, trace element distributions and speciation were determined by μXRF mapping and μXANES, respectively. Trace elements Ti and V were co-located with the Fe-rich "matrix" materials of the "inner" and "outer" nodule. In contrast, transition metals Ni, Cu, and Zn are primarily co-located with Mn within the "botryoidal" materials of the "inner" and "outer" nodule. These observations are consistent with a vast literature base demonstrating the affinity of oxyanions such as V for Fe oxyhydroxide minerals, and the affinity of divalent cations for Mn oxide minerals, in laboratory experiments and field observations (Brown et al., 1999; Cornell and Schwertmann, 2003; Nicholson and Eley, 1997). More specifically, our μXRF and μXAS observations build on previous investigations of hydrogenetic deposits that employed operationally defined, wet-chemical approaches. A strong correlation between Co, Ni, Cd, Zn, Cu and Mn in a "δ-MnO_2" phase was observed in hydroxylamine hydrochloride leaching experiments (Koschinsky and Halbach, 1995). Similarly, Ti and V were correlated with an "amorphous FeOOH" phase that dissolved in the presence of oxalic acid (Koschinsky and Halbach, 1995). Our X-ray microprobe observations confirm the interpretation of leaching experiments by showing that Ti and V are co-located with the Fe phases of the "matrix" throughout the SPG-2 nodule. In addition to co-location, Ti and V XANES results are most consistent with tetravalent Ti and pentavalent V in octahedral coordination to oxygen and adsorbed to Fe oxyhydroxides in the nodule. These associations did not vary along the growth radius of the nodule. Considering the evidence for mineral alteration over time, our Ti and V data indicate that trace metal speciation within the nodule is not over-written or erased as the minerals age to more stable phases.

Looking at the difference between "inner" and "outer" regions, we see that the Ti/Fe ratio (**Tables EA1** and **EA2**) decreases on going from "outer" to "inner", and the difference between the Ti/Fe ratio in matrix vs. botryoids increases. We speculate that as the Fe minerals age and become more crystalline, Ti is expelled from surface or edge sites. This effect would depend on which Fe minerals are involved, so might be expected to differ between matrix and botryoidal material. An analogous effect has been seen for Ni in the goethite fraction of lateritic soil by Dublet et al. (2015).

4.3 Fe isotope composition along the nodule

ACCEPTED MANUSCRIPT

The biogeochemical cycling of Fe in the oceans has important implications for the biological pump because Fe is a bio-limiting nutrient (Martin and Fitzwater, 1988). Thus, Fe bioavailability in marine environments through time could have influenced the regulation of the carbon cycle. Iron is delivered to the oceans from continents by rivers, glaciers, and windblown particles (dust), as well as by release from continental shelf sediments and hydrothermal venting (Raiswell and Canfield, 2012). These sources of Fe have different $\delta^{56/54}$Fe values that are further modified by chemical processes in the ocean (Beard et al., 2003; Chu et al., 2006; Conway and John, 2014; Dauphas and Rouxel, 2006; Horner et al., 2015; John et al., 2012; Radic et al., 2011; Scholz et al., 2014; Severmann et al., 2010). Hence, temporal Fe isotope variations in seawater, as recorded by FeMn hydrogenetic deposits, may help deciphering the variability of Fe sources to the oceans (Zhu et al., 2000; Chu et al., 2006; Horner et al., 2015). For instance, the Fe isotope composition in a Pacific hydrogenetic ferromanganese crust over 76 Ma shows that deep Fe sources (e.g. hydrothermal Fe) may have strongly influenced the Fe supply to the oceans over the Cenozoic (Horner et al., 2015). These findings questioned the general assumption that aeolian dust particles are the predominant source controlling the biogeochemical cycling of Fe in modern oceans. However, because precipitation and adsorption processes as well as mineralogy can fractionate Fe isotopes, our study provides a framework for understanding the relationships between fine-scale mineralogical variability in a ferromanganese nodule and preservation of Fe isotope composition from seawater.

The elemental composition for the nodule determined through bulk and micro-probe measurements, is typical of that reported for deep-sea hydrogenetic manganese nodules (Hein et al., 2013) and indicates that the source of metals to the nodule were from seawater sources, rather than sediments, during the time span we investigated. Fe isotope variations should be controlled by either changes in seawater Fe isotope composition, or by geochemical processes occurring in the nodule. The two main possible causes for fine-scale Fe isotope variability are the diffusion of Fe throughout the nodule and from seawater, and isotopic fractionation during exchange reactions and alteration to more stable phases associated with sorption reactions.

Based on a calculated diffusion coefficient for the nodule ($<1.10^{-12}$ cm^2/yr) (Henderson and Burton, 1999), we suggest that diffusion of Fe from seawater to the nodule cannot explain the homogeneous $\delta^{56/54}$Fe pattern. Our results rule out the effect of mineral alteration as a cause of measurable Fe isotopic fractionation. As discussed above, we did observe changes in the nodule mineralogy as well as variations in Fe contents and Mn/Fe ratios, as shown by µXRF and EMPA transects data in Figures 1-3, which could potentially have altered the original distribution of Fe

ACCEPTED MANUSCRIPT

732 isotopes along the nodule. However, while the Fe minerals in the nodule altered to more stable
733 phases over time, the Fe isotope composition, on a 2-3 mm sampling scale along the radius of
734 growth, remained constant throughout the nodule (- 0.12 ± 0.07 ‰). Despite a range of Fe isotope
735 fractionation factors that were measured during laboratory experiments involving adsorption
736 reactions and scavenging on Fe-phases (e.g.(Bullen et al., 2001; Johnson et al., 2005; Skulan et
737 al., 2002; Wu et al., 2011)), Horner et al. (2015) report that the isotopic fractionation caused by
738 the precipitation of dissolved seawater Fe (most likely in the form of Fe(III)-ligand) to
739 hydrogenetic ferromanganese crusts is $\Delta^{56/54}$Fe = + 0.77 ± 0.06 ‰. If we apply this fractionation
740 factor, $\Delta^{56/54}$Fe(seawater-nodule) = $\delta^{56/54}$Fe(seawater) - $\delta^{56/54}$Fe(nodule), to our hydrogenetic
741 nodule, then we obtain a $\delta^{56/54}$Fe source value of + 0.65 ‰ which is consistent with dissolved Fe
742 dominated by dust dissolution as reported in the Atlantic Ocean (e.g. + 0.70 ± 0.01 ‰;(Conway
743 and John, 2014)). Finally, implementation of our analytical approach to different type of nodules
744 (e.g. including nodules with a high diagenetic imprint) will help addressing the issue of the
745 influence of the nature of precursor Fe-phases on the fractionation of Fe isotopes during sorption
746 reactions and scavenging.
747
748
749
750
751 **5. Conclusions**
752 Our results provide a framework for addressing the degree to which deep-sea
753 ferromanganese nodules are archives of past oceanic conditions through trace element uptake and
754 preservation of chemical and isotopic features over time. First, in the Fe mineralogy, we observe
755 a transition from a low abundance of goethite in the "outer matrix" to higher abundance in the
756 "inner matrix" that is consistent with transformation of lepidocrocite- and ferrihydrite-like phases
757 to goethite over time. From these observations, we propose that the incipient Fe "matrix" is
758 composed of poorly ordered ferrihydrite and lepidocrocite phases. The initial trace element
759 uptake signatures should then be determined by the characteristics of the incipient phases and the
760 composition of the seawater at the sediment-water interface. As these phases are buried within
761 the nodule by subsequent mineral growth at the nodule surface, we observe evidence for mineral
762 transformation. Despite mineral transformation to more stable phases, the Ti and V coordination
763 chemistry and Fe stable isotope signatures are consistent along the growth radius of the SPG-2
764 nodule. These observations indicate that while the Fe mineral phases within nodules do undergo
765 alteration to more stable phases, the trace element speciation (with Ti and V as examples) and Fe

ACCEPTED MANUSCRIPT

isotope composition do not change in response. The primary implication of these findings is that buried layers of nodules are out of contact—geochemically—with surrounding seawater. Therefore, we conclude that the Fe minerals in MFNs are indeed faithful recorders of trace elements, at least Ti and V, over time.

6. Figure and table captions

Figure 1. Backscatter SEM images showing "outer" and “inner” regions. Red lines and crosses show locations of electron microprobe analyses displayed in Figure 4. The red line in Figure 1b transects an individual botryoidal structure.

Figure 2: Ternary diagram of Fe, Mn and (Ni+Co) x 10 (adapted from Bonatti et al., 1972) of Electron Microprobe data acquired along a transect through the whole nodule and bulk ICP-AES measurements on the nodule section. The distinction between “inner” and “outer” regions is explained in Table EA2 and in the text. This diagram allows to distinguish between three different fields (hydrothermal, hydrogenetic and diagenetic) indicating the predominant origin of the Fe/Mn-rich deposits formation. Selected literature data from Southeast Pacific nodules (green field) (Halbach et al., 1981) and Northeast Pacific (grey field) (Halbach et al. , 1981) are included for comparison.

Figure 3. Survey of the sample from "outer" (left) to “inner” regions. Top: Visible-light micrograph of the nodule. Middle: Tricolor-coded map showing Fe (red), Mn (green) and Ni (blue) in a strip extending from the surface of the nodule (left). Bottom: Averages Fe, Mn and Ni counts across the map. Ni counts are multiplied by 10 relative to Mn and Fe, for clarity. The micrograph and map are to the same field of view as the plot.

Figure 4: Plots of Ni/Fe (A), Co/Fe (B), Zn/Fe (C) and Ti/Fe (D) ratios versus Mn/Fe ratio of electron microprobe data acquired along two transects in the nodule "outer" and "inner" regions. Position of the transects in the nodule section are shown in Figure 1. See text for more explanation.

Figure. 5. µXRF maps of representative “inner” and "outer" regions showing several elements. Note that the distributions of V and Ti almost precisely match that of Fe. Zn is somewhat enriched in the matrix areas. Brighter pixels correspond to higher concentrations. Scale bars are 500 µm.

ACCEPTED MANUSCRIPT

Figure 6: Bicolor-coded maps of Ti (a,c) and V (b,d) in red, Fe in blue in "inner" and "outer regions. In map (e), where Fe is shown as red and Mn as cyan, the Fe-rich "matrix" appears in red and the "botryoidal" material in shades of blue-green. Scale bars are 1mm.

Figure 7. EXAFS data (thick lines, symbols) and fits (thin lines) for matrix spots and corresponding tricolor maps showing location of spots at which EXAFS data were taken. The fit for the "outer" is a three-shell fit as discussed in text. The fit for the "inner" is a linear combination fit to goethite and feroxyhite. Scale bars are 200μm.

Figure 8. Micro-XRD on "outer matrix" spots. Abscissa is $q=2\pi/d$ (nm^{-1}). The red and blue curves at top and bottom are simulated powder patterns for lepidocrocite and goethite, respectively. The red curve is flipped vertically to make it easier to trace the peak positions. The numbered peak locations for feroxyhite are from (Drits et al., 1993), classified by intensity. Sharp peaks marked with asterisks match albite.

Figure 9. Tricolor-coded μXRF maps showing botryoidal spots on which spectroscopy was performed in "outer" (a) and "inner" (b) regions. Scale bars are 200 μm (a) and 800 μm (b).

Figure 10. Fit of Inner spot 5 (see bottom panel of Figure 9) to Fe-O, two Fe-Fe shells and goethite. The top panel shows the contributions of each shell (divided by 2). The bottom panel shows the magnitude and imaginary parts of the FT for data and fit.

Figure 11. XANES for Ti in "inner" matrix (average of 3 spots, black) compared with that of ilmenite (red).

Figure 12. V K-XANES spectra for the ITFA end-members found in the nodule (solid black, solid red), V(V) on 2-line ferrihydrite (dashed black), and V(IV) on δ-MnO_2 (dashed red). The inset shows the pre-edge region on an expanded scale.

Figure 13. Correlation between fitted fraction of ITFA1 end-member and the ratio of counts in the Fe to Mn XRF channels. Small tricolor (red=Fe, green=Mn, blue=Ni) maps show where points were taken. Maps Inner2 and Outer2 were taken in the same run on the same thin-section;

ACCEPTED MANUSCRIPT

map Inner1 came from a different run and thin section. Map Inner1 is 777 µm tall; maps Inner2 and Outer2 are 2000µm tall.

Figure 14. Fits of the ITFA0 (black) and ITFA1 (red) end-members to δ-MnO_2-sorbed V, 2-line ferrihydrite-sorbed V and $LaCl_3$•7H2O. Data and residuals are shown in points and fits in solid lines.

Table 1. Wet chemical analyses of the nodule section measured by ICP-AES

Table EA1 (Electronic Annex) Be isotopes (a) and calculation of the nodule growth rate (b).

Table EA2 (Electronic Annex). Electron microprobe analyses (in wt %) of 10 transects through the whole nodule section (from "outer" to "inner" nodule) and elemental ratios.

Table EA3 (Electronic Annex). Electron microprobe analyses (in wt %) of two micro-transects in the "outer" and "inner" nodule regions and elemental ratios

7. Acknowledgments

We thank the science team, crew, and Chief Scientist Steven D'Hondt of the KNOX02RR cruise for access to the South Pacific Gyre. We thank Tristan Horner for helpful discussions of the manuscript; Lindsey Briscoe for measuring the XRD pattern of feroxyhite (Characterization Facility, University of Minnesota, which receives partial support from NSF through the MRSEC program); Fred Davis for measuring the elemental composition by electron microprobe (Electron Microprobe Laboratory, University of Minnesota), Shahida Quazi for assistance at ALS BL 10.3.2, and Terhuhiko Kashiwabara for discussions and reference spectra for V and La, Emmanuel Ponzevera, Yoan Germain and Celine Liorzou for technical assistance at Ifremer-IUEM, and Purdue University's PRIME Lab for ^{10}Be AMS measurements.. The Advanced Light Source is supported by the Director, Office of Science, Office of Basic Energy Sciences, of the U.S. Department of Energy under Contract No. DE-AC02-05CH11231. OR and BG thank funding sources from ANR-10-LABX-19-01 and Institut Carnot - EDROME.

REFERENCES

ACCEPTED MANUSCRIPT

867 Albarède, F. and Beard, B. (2004) Analytical methods for non-traditional isotopes. Reviews in
868 mineralogy and geochemistry 55, 113-152.
869 Aplin, A.C. and Cronan, D.S. (1985) Ferromanganese oxide deposits from the Central Pacific
870 Ocean, II. Nodules and associated sediments. Geochim. Cosmochim. Acta 49, 437-451.
871 Axelsson, M.D., Rodushkin, I., Ingri, J. and Ohlander, B. (2002) Multielemental analysis of Mn-
872 Fe nodules by ICP-MS: optimisation of analytical method. Analyst 127, 76-82.
873 Banakar, V.K. and Tarkian, M. (1991) Genesis and growth of internal microstructures of
874 manganese nodules. Indian Journal of Marine Sciences 20, 20-24.
875 Banerjee, R., Roy, S., Dasgupta, S., Mukhopadhyay, S. and Miura, H. (1999) Petrogenesis of
876 ferromanganese nodules from east of the Chagos Archipelago, Central Indian Basin, Indian
877 Ocean. Marine Geology 157, 145-158.
878 Baturin, G.N. and Savenko, V.S. (1989) Growth rates of deep- water iron-manganese nodules.
879 Oceanology 29, 334-342.
880 Beard, B.L., Johnson, C.M., Von Damm, K.L. and Poulson, R.L. (2003) Iron isotope constraints
881 on Fe cycling and mass balance in oxygenated Earth oceans. Geology 31, 629-632.
882 Bhat, S., Krishnaswami, S., Lal, D., Rama, D. and Somayajulu, B. (1973) Radiometric and trace
883 element studies of ferromanganese nodules, Proc. Symp. Hydrogeochemistry and
884 Biogeochemistry, pp. 443-462.
885 Birnie, A.C. and Paterson, E. (1991) The mineralogy and morphology of iron and manganese
886 oxides in an imperfectly-drained Scottish soil. Geoderma 50, 219-237.
887 Brown, G.E., Jr, Henrich, V.E., Casey, W.H., Clark, D.L., Eggleston, C., Felmy, A., Goodman,
888 D.W., Gratzel, M., Maciel, G., McCarthy, M.I., Nealson, K.H., Sverjensky, D.A., Toney, M.F.
889 and Zachara, J.M. (1999) Metal oxide surfaces and their interactions with aqueous solutions and
890 microbial organisms. Chemical Reviews 99, 77-174.
891 Bullen, T.D., White, A.F., Childs, C.W., Vivit, D.V. and Schulz, M.S. (2001) Demonstration of
892 significant abiotic iron isotope fractionation in nature. Geology 29, 699-702.
893 Calvert, S.E. and Cronan, D.S. (1978) Geochemistry of oceanic ferromanganese deposits.
894 Philosophical Transactions of the Royal Society London A 290, 43-73.
895 Carlson, L. and Schwertmann, U. (1980) Natural occurrence of feroxyhite (δ'-FeOOH). Clays and
896 Clay Minerals 28, 272-280.
897 Chmeleff, J., von Blanckenburg, F., Kossert, K. and Jakob, D. (2010) Determination of the ^{10}Be
898 half-life by multicollector ICP-MS and liquid scintillation counting. Nuclear Instruments and
899 Methods in Physics Research Section B: Beam Interactions with Materials and Atoms 268, 192-
900 199.
901 Chu, N.-C., Johnson, C., Beard, B., German, C., Nesbitt, R., Frank, M., Bohn, M., Kubik, P.,
902 Usui, A. and Graham, I. (2006) Evidence for hydrothermal venting in Fe isotope compositions of
903 the deep Pacific Ocean through time. Earth and Planetary Science Letters 245, 202-217.
904 Chukhrov, F., Zvyagin, B., Gorshkov, A., Yermilova, L., Korovushkin, V., Rudnitskaya, Y.S.
905 and Yakubovskaya, N.Y. (1977) Feroxyhyte, a new modification of FeOOH. International
906 Geology Review 19, 873-890.
907 Conway, T.M. and John, S.G. (2014) Quantification of dissolved iron sources to the North
908 Atlantic Ocean. Nature 511, 212-215.
909 Cornell, R.M., R, G. and Schneider, W. (1992) The effect of nickel on the conversion of
910 amorphous iron(III) hydroxide into more crystalline iron oxides in alkaline media. J. Chem. Tech.
911 Biotechnol. 53, 73-79.
912 Cornell, R.M. and Schwertmann, U. (2003) The Iron Oxides: Structure, properties, reactions,
913 occurrences and uses, Second, completely revised and extended ed. Wiley-VCH, Darmstadt,
914 Germany.
915 Cronan, D.S. (1975) Manganese nodules and other ferromangese oxide deposits from Atlantic
916 Ocean. Journal of Geophysical Research-Oceans and Atmospheres 80, 3831-3837.

ACCEPTED MANUSCRIPT

D'Hondt, S., Spivack, A.J., Pockalny, R., Ferdelman, T.G., Fischer, J.P., Kallmeyer, J., Abrams, L.J., Smith, D.C., Graham, D., Hasiuk, F., Schrum, H. and Stancin, A.M. (2009) Subseafloor sedimentary life in the South Pacific Gyre. Proceedings of the National Academy of Sciences 106, 11651-11656.

Dauphas, N. and Rouxel, O. (2006) Mass spectrometry and natural variations of iron isotopes. Mass Spectrometry Reviews 25, 515-550.

de Lange, G.J., van Os, B. and Poorter, R. (1992) Geochemical composition and inferred accretion rates of sediments and manganese nodules from a submarine hill in the Madeira Abyssal Plain, eastern North Atlantic. Marine Geology 109, 171-194.

Dideriksen, K., Baker, J.A. and Stipp, S.L.S. (2006) Iron isotopes in natural carbonate minerals determined by MC-ICP-MS with a Fe-58-Fe-54 double spike. Geochimica Et Cosmochimica Acta 70, 118-132.

Drits, V., Sakharov, B. and Manceau, A. (1993) Structure of feroxyhite as determined by simulation of X-ray diffraction curves. Clay Minerals 28, 209-209.

Dublet, G., Juillot, F., Morin, G., Fritsch, E., Fandeur, D. and Brown, G.E. (2015) Goethite aging explains Ni depletion in upper units of ultramafic lateritic ores from New Caledonia. Geochim. Cosmochim. Acta 160, 1-15.

Dymond, J., Lyle, M.W., Finney, B., Piper, D.Z., Murphy, K., Conard, R. and Pisias, N. (1984) Ferromanganese nodules from MANOP Sites H, S, and R - Control of mineralogical and chemical composition by multiple accretionary processes. Geochim. Cosmochim. Acta 48, 931-949.

Ebert, K., Willenbring, J., Norton, K.P., Hall, A. and Hättestrand, C. (2012) Meteoric ^{10}Be concentrations from saprolite and till in northern Sweden: Implications for glacial erosion and age. Quaternary Geochronology 12, 11-22.

Eickhoff, M., Obst, M., Schröder, C., Hitchcock, A.P., Tyliszczak, T., Martinez, R.E., Robbins, L.J., Konhauser, K.O. and Kappler, A. (2014) Nickel partitioning in biogenic and abiogenic ferrihydrite: The influence of silica and implications for ancient environments. Geochim. Cosmochim. Acta 140, 65-79.

Elderfield, H., Hawkesworth, C.J., Greaves, M.J. and Calvert, S.E. (1981) Rare-earth element zonation in Pacific ferromanganese nodules. Geochim. Cosmochim. Acta 45, 1231-1234.

Frierdich, A.J. and Catalano, J.G. (2012) Controls on Fe(II)-activated trace element release from goethite and hematite. Environ. Sci. Technol. 46, 1519-1526.

Frierdich, A.J., Luo, Y. and Catalano, J.G. (2011) Trace element cycling through iron oxide minerals during redox-driven dynamic recrystallization. Geology 39, 1083-1086.

Gradstein, F. and Ogg, J. (2002) Future directions in stratigraphy. Episodes 25, 203-208.

Graham, I., Carter, R., Ditchburn, R. and Zondervan, A. (2004) Chronostratigraphy of ODP 181, Site 1121 sediment core (Southwest Pacific Ocean), using ^{10}Be/^{9}Be dating of entrapped ferromanganese nodules. Marine geology 205, 227-247.

Halbach, P. and Puteanus, D. (1984) The influence of the carbonate dissolution rate on the growth and composition of Co-rich ferromanganese crusts from Central Pacific seamount areas. Earth and Planetary Science Letters 68, 73-87.

Halbach, P., Scherhag, C., Hebisch, U. and Marchig, V. (1981) Geochemical and mineralogical control of different genetic types of deep-sea nodules from the Pacific Ocean. Mineralium deposita 16, 59-84.

Hammersley, A. (1997) FIT2D: an introduction and overview. European Synchrotron Radiation Facility Internal Report ESRF97HA02T.

Heggie, D., Kahn, D. and Fischer, K. (1986) Trace metals in metalliferous sediments, MANOP Site M: interfacial pore water profiles. Earth and Planetary Science Letters 80, 106-116.

Hein, J.R., Koschinsky, A. and Halliday, A.N. (2003) Global occurrence of tellurium-rich ferromanganese crusts and a model for the enrichment of tellurium. Geochim. Cosmochim. Acta 67, 1117-1127.

ACCEPTED MANUSCRIPT

968 Hein, J.R., Mizell, K., Koschinsky, A. and Conrad, T.A. (2013) Deep-ocean mineral deposits as a
969 source of critical metals for high- and green-technology applications: Comparison with land-
970 based resources. Ore Geology Reviews 51, 1-14.
971 Henderson, G.M. and Burton, K.W. (1999) Using ($^{234}U/^{238}U$) to assess diffusion rates of isotope
972 tracers in ferromanganese crusts. Earth and Planetary Science Letters 170, 169-179.
973 Horner, T.J., Williams, H.M., Hein, J.R., Saito, M.A., Burton, K.W., Halliday, A.N. and Nielsen,
974 S.G. (2015) Persistence of deeply sourced iron in the Pacific Ocean. Proceedings of the National
975 Academy of Sciences, 201420188.
976 Jahnke, R.A. (1996) The global ocean flux of particulate organic carbon: Areal distribution and
977 magnitude. Global biogeochemical cycles 10, 71-88.
978 John, S.G., Mendez, J., Moffett, J. and Adkins, J. (2012) The flux of iron and iron isotopes from
979 San Pedro Basin sediments. Geochim. Cosmochim. Acta 93, 14-29.
980 Johnson, C.M., Roden, E.E., Welch, S.A. and Beard, B.L. (2005) Experimental constraints on Fe
981 isotope fractionation during magnetite and Fe carbonate formation coupled to dissimilatory
982 hydrous ferric oxide reduction. Geochim. Cosmochim. Acta 69, 963-993.
983 Klinkhammer, G., Heggie, D.T. and Graham, D.W. (1982) Metal diagenesis in oxic marine-
984 sediments. Earth and Planetary Science Letters 61, 211-219.
985 Korschinek, G., Bergmaier, A., Faestermann, T., Gerstmann, U., Knie, K., Rugel, G., Wallner,
986 A., Dillmann, I., Dollinger, G. and Von Gostomski, C.L. (2010) A new value for the half-life of
987 ^{10}Be by Heavy-Ion Elastic Recoil Detection and liquid scintillation counting. Nuclear Instruments
988 and Methods in Physics Research Section B: Beam Interactions with Materials and Atoms 268,
989 187-191.
990 Koschinsky, A. and Halbach, P. (1995) Sequential leaching of marine ferromanganese
991 precipitates: Genetic implications. Geochim. Cosmochim. Acta 59, 5113-5132.
992 Koschinsky, A. and Hein, J.R. (2003) Uptake of elements from seawater by ferromanganese
993 crusts: solid-phase associations and seawater speciation. Marine geology 198, 331-351.
994 Koschinsky, A., Stascheit, A., Bau, M. and Halbach, P. (1997) Effects of phosphatization on the
995 geochemical and mineralogical composition of marine ferromanganese crusts. Geochim.
996 Cosmochim. Acta 61, 4079-4094.
997 Larson, R.L., Pockalny, R.A., Viso, R.F., Erba, E., Abrams, L.J., Luyendyk, B.P., Stock, J.M. and
998 Clayton, R.W. (2002) Mid-Cretaceous tectonic evolution of the Tongareva triple junction in the
999 southwestern Pacific Basin. Geology 30, 67-70.
1000 Latta, D.E., Gorski, C.A. and Scherer, M.M. (2012) Influence of Fe^{2+}-catalyzed iron oxide
1001 recrystallization on metal cycling. Biochemical Society Transations 40, 1191-1197.
1002 Levasseur, S., Frank, M., Hein, J. and Halliday, A. (2004) The global variation in the iron isotope
1003 composition of marine hydrogenetic ferromanganese deposits: implications for seawater
1004 chemistry? Earth and Planetary Science Letters 224, 91-105.
1005 Lu, B., Guo, H., Li, P., Liu, H., Wei, Y. and Hou, D. (2011) Comparison study on transformation
1006 of iron oxyhydroxides: Based on theoretical and experimental data. Journal of Solid State
1007 Chemistry 184, 2139-2144.
1008 Manceau, A., Lanson, M. and Takahashi, Y. (2014) Mineralogy and crystal chemistry of Mn, Fe,
1009 Co, Ni, and Cu in a deep-sea Pacific polymetallic nodule. Am. Mineral. 99, 2068-2083.
1010 Manceau, A., Marcus, M.A. and Tamura, N. (2002) Quantitative speciation of heavy metals in
1011 soils and sediments by synchrotron X-ray techniques, in: Fenter, P.A., Rivers, M.L., Sturchio,
1012 N.C., Sutton, S.R. (Eds.), Applications of Synchrotron Radiation in Low-Temperature
1013 Geochemistry and Environmental Science. Mineralogical Society of America, Washington, DC,
1014 pp. 341-428.
1015 Marcus, M.A., MacDowell, A.A., Celestre, R., Manceau, A., Miller, T., Padmore, H.A. and
1016 Sublett, R.E. (2004a) Beamline 10.3.2 at ALS: a hard X-ray microprobe for environmental and
1017 materials sciences. J. Synchrotron Radiation 11, 239-247.

ACCEPTED MANUSCRIPT

1018 Marcus, M.A., Manceau, A. and Kersten, M. (2004b) Mn, Fe, Zn and As speciation in a fast-
1019 growing ferromanganese marine nodule. Geochim. Cosmochim. Acta 68, 3125-3136.
1020 Marcus, M.A., Westphal, A.J. and Fakra, S.C. (2008) Classification of Fe-bearing species from
1021 K-edge XANES data using two-parameter correlation plots. J. Synchrotron Radiation 15, 463-
1022 468.
1023 Martin-Barajas, A., Lallier-Verges, E. and Leclaire, L. (1991) Characteristics of manganese
1024 nodules from the Central Indian Basin: Relationship with the sedimentary environment. Marine
1025 Geology 101, 249-265.
1026 Martin, J.H. and Fitzwater, S. (1988) Iron deficiency limits phytoplankton growth in the north-
1027 east Pacific subarctic. Nature 331, 947-975.
1028 McKenzie, R. (1971) The synthesis of birnessite, cryptomelane, and some other oxides and
1029 hydroxides of manganese. Mineralogical Magazine 38, 493-502.
1030 Morford, J.L. and Emerson, S. (1999) The geochemistry of redox sensitive trace metals in
1031 sediments. Geochim. Cosmochim. Acta 63, 1735-1750.
1032 Murad, E. and Schwertmann, U. (1988) Iron oxide mineralogy of some deep-sea ferromanganese
1033 crusts. Am. Mineral. 73, 1395-1400.
1034 Navrotsky, A., Mazeina, L. and Majzlan, J. (2008) Size-driven structural and thermodynamic
1035 complexity in iron oxides. Science 319, 1635-1638.
1036 Newville, M. (2001) IFEFFIT: interactive XAFS analysis and FEFF fitting. J. Synchrotron
1037 Radiation 8, 322-324.
1038 Nicholson, K. and Eley, M. (1997) Geochemistry of manganese oxides: metal adsorption in
1039 freshwater and marine environments, in: Nicholson, K., Hein, J.R., Bühn, B., Dasgupta, S. (Eds.),
1040 Manganese Mineralization: Geochemistry and Mineralogy of Terrestrial and Marine Deposits.
1041 Geological Society Special Publication No. 119. The Geological Society, London, pp. 309-326.
1042 Peacock, C.L. (2009) Physiochemical controls on the crystal-chemistry of Ni in birnessite:
1043 Genetic implications for ferromanganese precipitates. Geochim Cosmochim Acta 73, 3568-3578.
1044 Radic, A., Lacan, F. and Murray, J.W. (2011) Iron isotopes in the seawater of the equatorial
1045 Pacific Ocean: new constraints for the oceanic iron cycle. Earth and Planetary Science Letters
1046 306, 1-10.
1047 Raiswell, R. and Canfield, D.E. (2012) The iron biogeochemical cycle past and present.
1048 Geochemical Perspectives 1, 1-2.
1049 Ravel, B. and Newville, M. (2005) ATHENA, ARTEMIS, HEPHAESTUS: data analysis for X-
1050 ray absorption spectroscopy using IFEFFIT. J. Synchrotron Radiation 12, 537-541.
1051 Rouxel, O., Shanks III, W.C., Bach, W. and Edwards, K.J. (2008) Integrated Fe-and S-isotope
1052 study of seafloor hydrothermal vents at East Pacific Rise 9–10 N. Chemical Geology 252, 214-
1053 227.
1054 Rouxel, O.J., Bekker, A. and Edwards, K.J. (2005) Iron isotope constraints on the Archean and
1055 Paleoproterozoic ocean redox state. Science 307, 1088-1091.
1056 Sawlan, J.J. and Murray, J.W. (1983) Trace-metal remobilization in the interstitial waters of red
1057 clay and hemipelagic marine-sediments. Earth and Planetary Science Letters 64, 213-230.
1058 Scholz, F., Severmann, S., McManus, J., Noffke, A., Lomnitz, U. and Hensen, C. (2014) On the
1059 isotope composition of reactive iron in marine sediments: Redox shuttle versus early diagenesis.
1060 Chemical Geology 389, 48-59.
1061 Schwertman, U. and Cornell, R. (1991) Iron Oxides in the Laboratory Preparation and
1062 Characterization. VCH Publishers.
1063 Schwertmann, U. and Cornell, R.M. (2000) The Iron Oxides, Iron oxides in the laboratory.
1064 Preparation and characterization, Second, completely revised and extended ed. Wiley-VCH, pp.
1065 4-18.
1066 Segl, M., Mangini, A., Beer, J., Bonani, G., Suter, M. and Wölfli, W. (1989) Growth rate
1067 variations of manganese nodules and crusts induced by paleoceanographic events.
1068 Paleoceanography 4, 511-530.

ACCEPTED MANUSCRIPT

Severmann, S., McManus, J., Berelson, W.M. and Hammond, D.E. (2010) The continental shelf benthic iron flux and its isotope composition. Geochim. Cosmochim. Acta 74, 3984-4004.
Skulan, J.L., Beard, B.L. and Johnson, C.M. (2002) Kinetic and equilibrium Fe isotope fractionation between aqueous Fe (III) and hematite. Geochim. Cosmochim. Acta 66, 2995-3015.
Somayajulu, B. (2000) Growth rates of oceanic manganese nodules: implications to their genesis, palaeo-earth environment and resource potential. Current Science 78, 300-308.
Takahashi, Y., Manceau, A., Geoffroy, N., Marcus, M.A. and Usui, A. (2007) Chemical and structural control of the partitioning of Co, Ce, and Pb in marine ferromanganese oxides. Geochim. Cosmochim. Acta 71, 984-1008.
Takahashi, Y., Shimizu, H., Kagi, H., Yoshida, H., Usui, A. and Nomura, M. (2000) A new method for the determination of Ce^{III}/Ce^{IV} ratios in geological materials; application for weathering, sedimentary and diagenetic processes. Earth and Planetary Science Letters 182, 201-207.
Tanaka, T., Nishimura, Y., Kawasaki, S.-i., Funabiki, T. and Yoshida, S. (1987) X-Ray absorption spectroscopy (EXAFS/XANES) evidence for the preferential formation of isolated VO_4 species on highly photoactive V_2O_5/SiO_2 catalysts. Journal of the Chemical Society, Chemical Communications, 506-508.
Toner, B.M., Berquo, T.S., Michel, F.M., Sorensen, J.V., Templeton, A.S. and Edwards, K.J. (2012) Mineralogy of iron microbial mats from Loihi Seamount. Frontiers in Microbiological Chemistry 3, 1-18.
Toner, B.M., Santelli, C.M., Marcus, M.A., Wirth, R., Chan, C.S., McCollom, T.M., Bach, W. and Edwards, K.J. (2009) Biogenic iron oxyhydroxide formation at Mid-Ocean Ridge hydrothermal vents: Juan de Fuca Ridge. Geochim. Cosmochim. Acta 73, 388-403.
Verlaan, P.A., Cronan, D.S. and Morgan, C.L. (2004) A comparative analysis of compositional variations in and between marine ferromanganese nodules and crusts in the South Pacific and their environmental controls. Progress in Oceanography 63, 125-158.
Villalobos, M., Toner, B., Bargar, J. and Sposito, G. (2003) Characterization of the manganese oxide produced by Pseudomonas putida strain MnB1. Geochim. Cosmochim. Acta 67, 2649-2662.
Wang, X., Schloßmacher, U., Wiens, M., Schröder, H.C. and Müller, W.E. (2009) Biogenic origin of polymetallic nodules from the Clarion-Clipperton zone in the Eastern Pacific Ocean: electron microscopic and EDX evidence. Marine Biotechnology 11, 99-108.
Willenbring, J.K. and von Blanckenburg, F. (2010a) Long-term stability of global erosion rates and weathering during late-Cenozoic cooling. Nature 465, 211-214.
Willenbring, J.K. and von Blanckenburg, F. (2010d) Meteoric cosmogenic Beryllium-10 adsorbed to river sediment and soil: Applications for Earth-surface dynamics. Earth-Science Reviews 98, 105-122.
Wong, J., Lytle, F., Messmer, R. and Maylotte, D. (1984) K-edge absorption spectra of selected vanadium compounds. Physical Review B 30, 5596.
Wu, L., Beard, B.L., Roden, E.E. and Johnson, C.M. (2011) Stable iron isotope fractionation between aqueous Fe (II) and hydrous ferric oxide. Environ. Sci. Technol. 45, 1847-1852.
Yoshikawa, K. (1991) The relationship between manganese minerals and metallic elements in deep-sea manganese nodules. Marine Geology 101, 267-286.
Zhu, X.K., O'Nions, R.K., Guo, Y.L. and Reynolds, B.C. (2000) Secular variation of iron isotopes in North Atlantic Deep Water. Science 287, 2000-2002.

ACCEPTED MANUSCRIPT

Table 1: Bulk chemical analyses of the nodule section measured by ICP-AES and $\delta^{56/54}$Fe values (‰) measured by MC-ICP-MS.

Nodule section #	Distance from nodule surface (mm)**	Al/Fe	Ba/Fe	Ca/Fe	Ce/Fe	Co/Fe	Cu/Fe	K/Fe	La/Fe	Mg/Fe	Mn/Fe	Mo/Fe	Na/Fe	Ni/Fe	P/Fe	Sr/Fe	Ti/Fe	Zn/Fe	Cu/Ni	$\delta^{56/54}Fe_{IRMM-1}$	2sd***
N1 (Outer)	3	0.184	0.0085	0.119	0.0114	0.035	0.0096	0.047	0.0015	0.0843	1.14	0.0019	0.123	0.0217	0.017	0.0064	0.106	0.0036	0.45	-0.16	0.09
N2	6	0.165	0.0081	0.109	0.0093	0.030	0.0076	0.040	0.0014	0.0634	0.93	0.0016	0.095	0.0138	0.016	0.0057	0.105	0.0030	0.55	-0.09	0.09
N3	8	0.214	0.0078	0.122	0.0096	0.034	0.0089	0.054	0.0015	0.0763	1.04	0.0018	0.107	0.0184	0.019	0.0060	0.104	0.0035	0.48	-0.17	0.09
N4	10	0.191	0.0080	0.150	0.0095	0.031	0.0095	0.040	0.0015	0.0714	1.10	0.0018	0.106	0.0215	0.022	0.0060	0.095	0.0038	0.44	-0.14	0.09
N5	12.5	0.199	0.0083	0.150	0.0104	0.034	0.0094	0.032	0.0014	0.0747	1.25	0.0022	0.115	0.0241	0.016	0.0066	0.087	0.0039	0.39	-0.07	0.09
N6	13.5	0.215	0.0077	0.141	0.0096	0.028	0.0084	0.032	0.0013	0.0677	1.04	0.0019	0.099	0.0182	0.016	0.0060	0.079	0.0037	0.46	-0.10	0.09
N7	14.5	0.227	0.0072	0.126	0.0089	0.027	0.0084	0.037	0.0011	0.0672	1.02	0.0020	0.103	0.0169	0.015	0.0056	0.071	0.0038	0.50	-0.16	0.09
N8	16	0.193	0.0076	0.112	0.0100	0.031	0.0085	0.038	0.0012	0.0688	1.02	0.0021	0.098	0.0179	0.015	0.0058	0.076	0.0040	0.48	-0.09	0.09
N9	18	0.188	0.0071	0.110	0.0111	0.034	0.0082	0.033	0.0012	0.0724	1.02	0.0022	0.092	0.0183	0.016	0.0056	0.083	0.0040	0.45	-0.08	0.09
N10 (Inner)	19.5	0.160	0.0073	0.099	0.0133	0.026	0.0083	0.022	0.0012	0.0682	0.92	0.0022	0.084	0.0178	0.017	0.0055	0.075	0.0043	0.46	-0.11	0.09
USGS Nod-P-1	-	0.379	0.0448	0.395	0.0064	0.041	0.2113	0.193	0.0021	0.3360	5.10	0.0106	0.304	0.2504	0.027	0.0114	0.052	0.0306	0.84	-0.49	0.07
USGS Nod-A-1	-	0.197	0.0140	1.129	0.0079	0.031	0.0103	0.048	0.0013	0.2647	1.73	0.0035	0.081	0.0634	0.041	0.0145	0.033	0.0059	0.16	-0.40	0.09

* Concentrations are given in grams of element per gram of Fe (i.e. Element/Fe ratios).

** Distance from outer nodule is reported as the distance from the top surface of the nodule.

*** 2sd was dtermined on replicate measurements of the Fe isotopic standard IRMM-14. See text for explanations.

ACCEPTED MANUSCRIPT

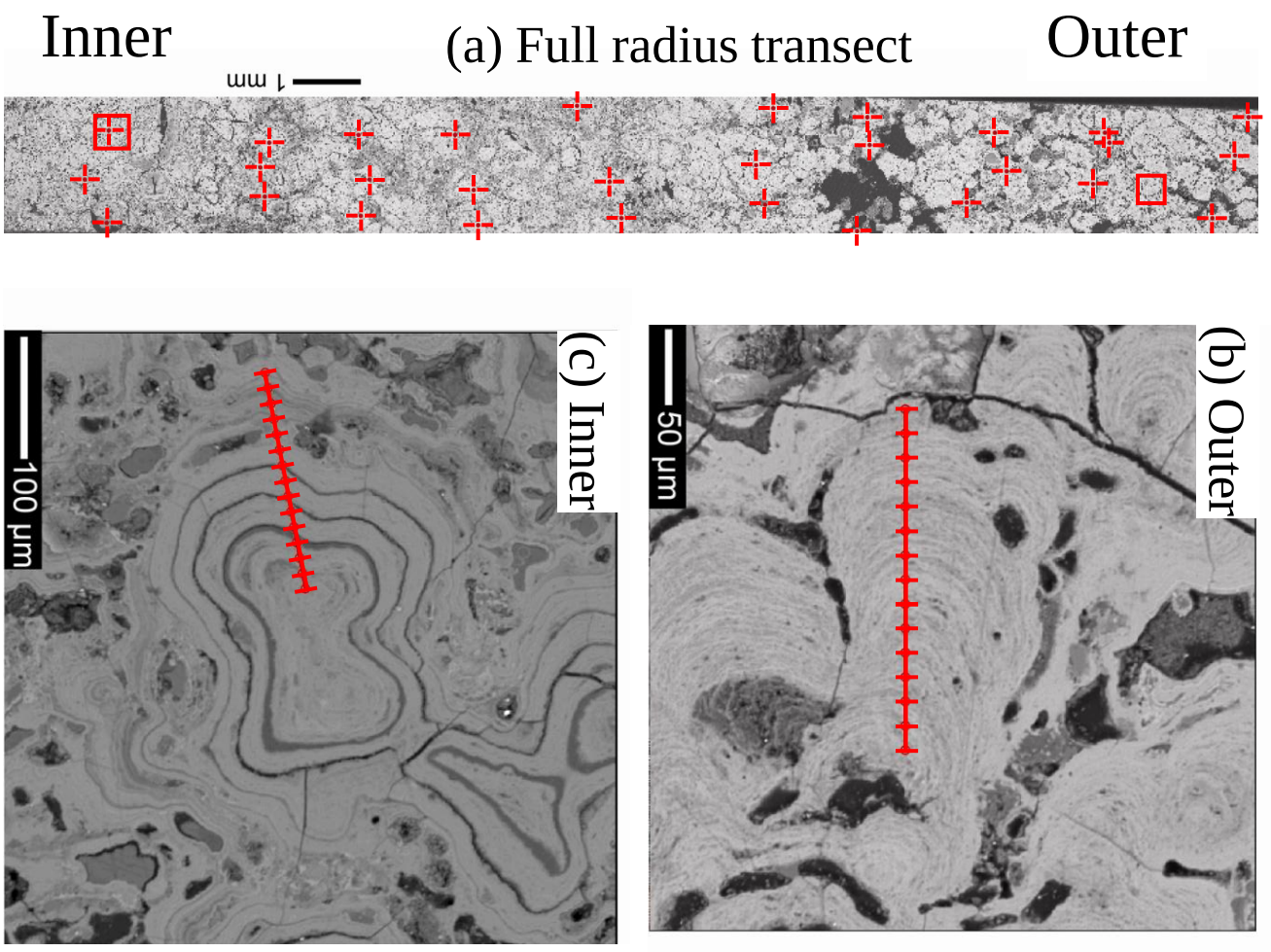
Inner
(a) Full radius transect
Outer
1 mm
(c) Inner
100 µm
(b) Outer
50 µm

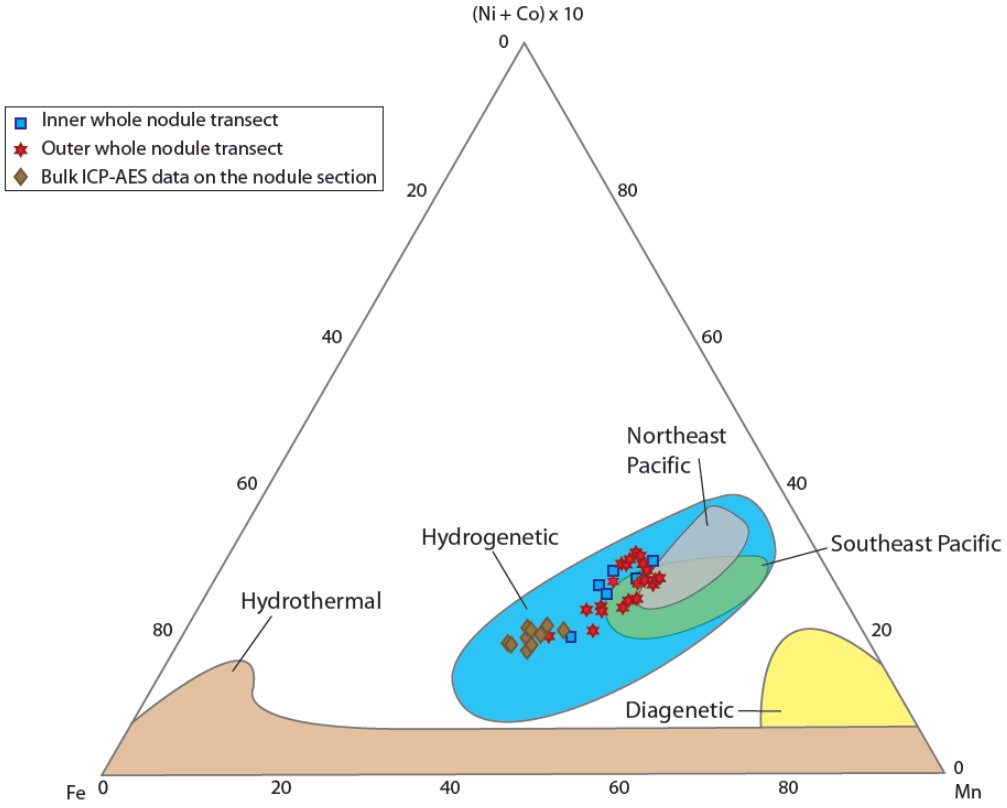
(Ni + Co) x 10
0
20
40
60
80
Inner whole nodule transect
Outer whole nodule transect
Bulk ICP-AES data on the nodule section
Northeast Pacific
Hydrogenetic
Southeast Pacific
Hydrothermal
Diagenetic
Fe
Mn

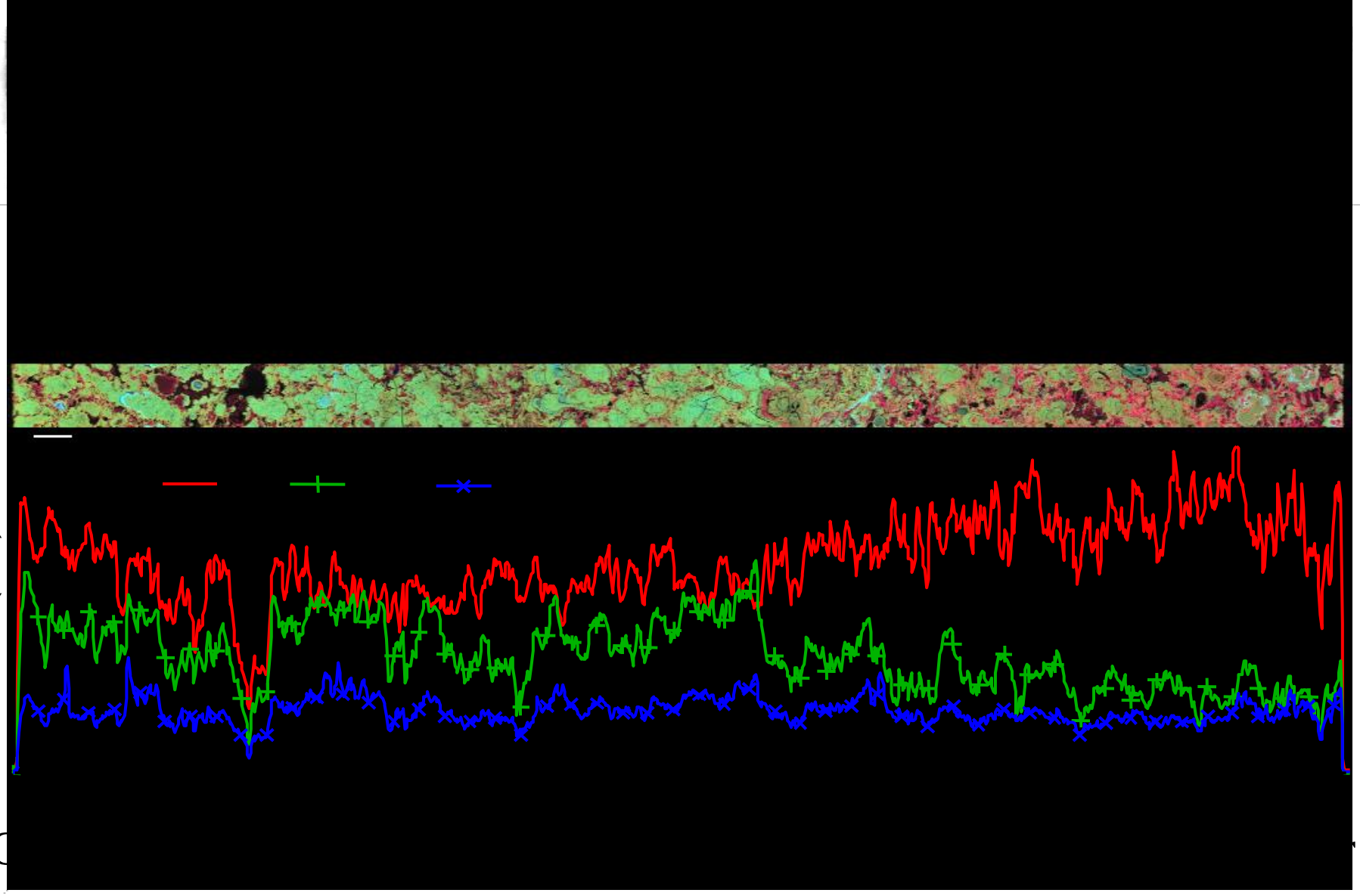
Counts (AU)

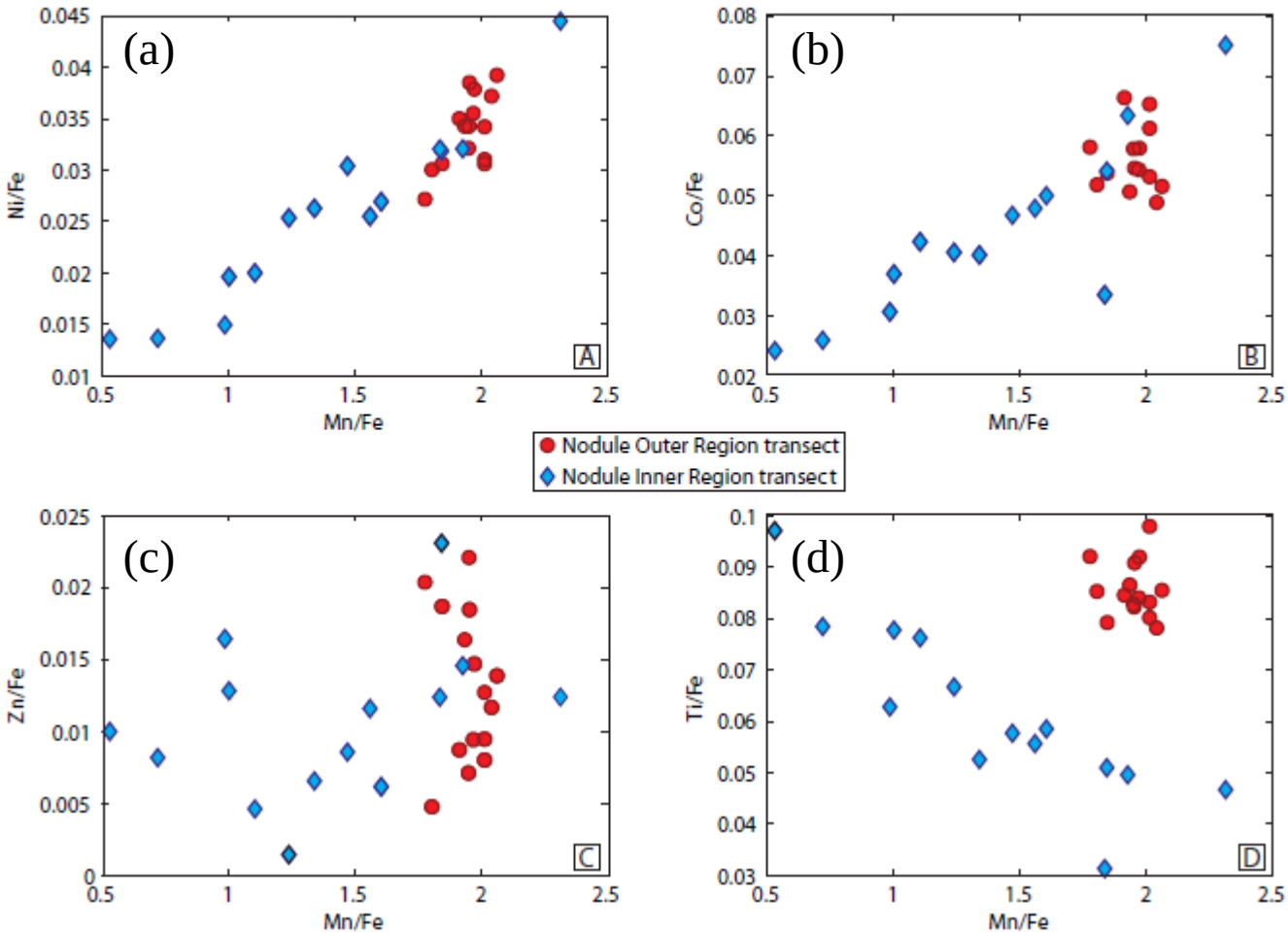
(a)
Ni/Fe
Mn/Fe
A
(b)
Co/Fe
Mn/Fe
B
Nodule Outer Region transect
Nodule Inner Region transect
(c)
Zn/Fe
Mn/Fe
C
(d)
Ti/Fe
Mn/Fe
D

Inner

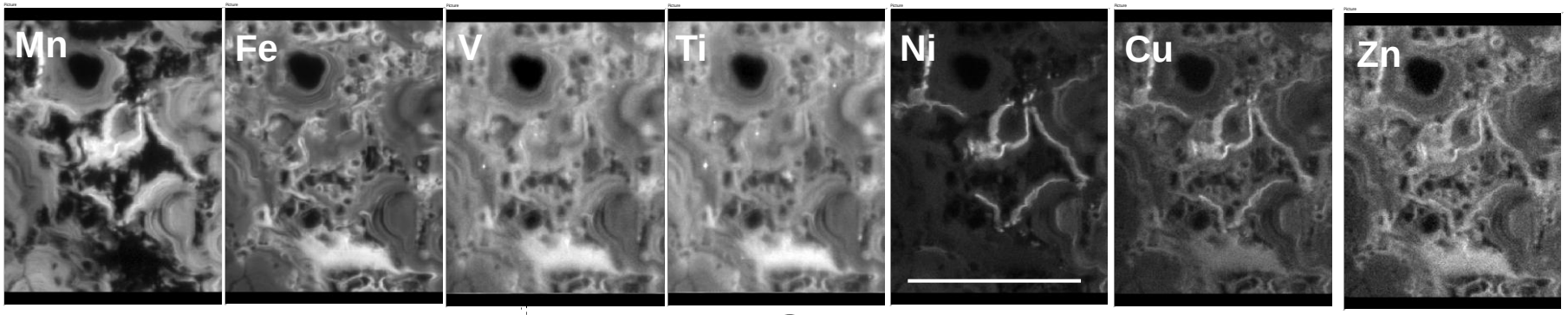

Outer

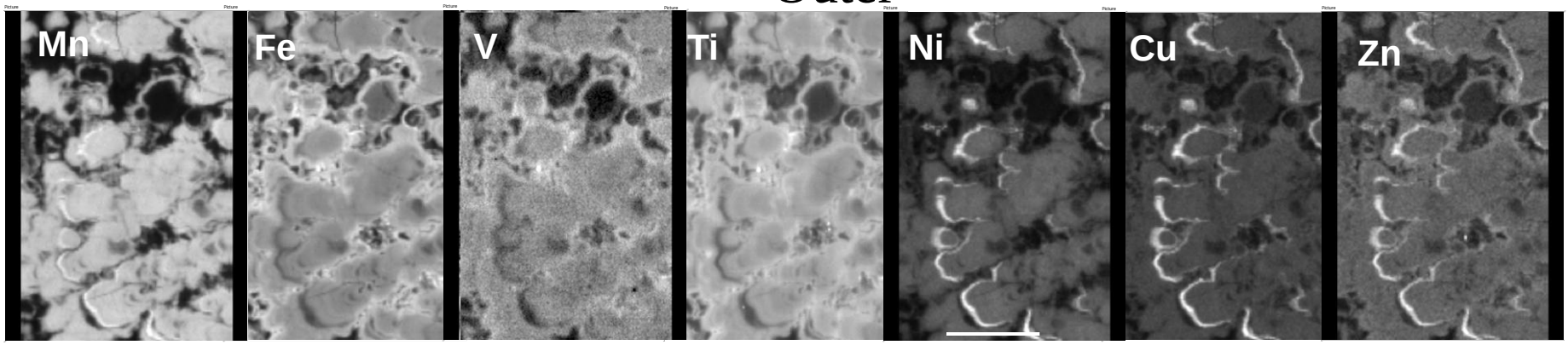

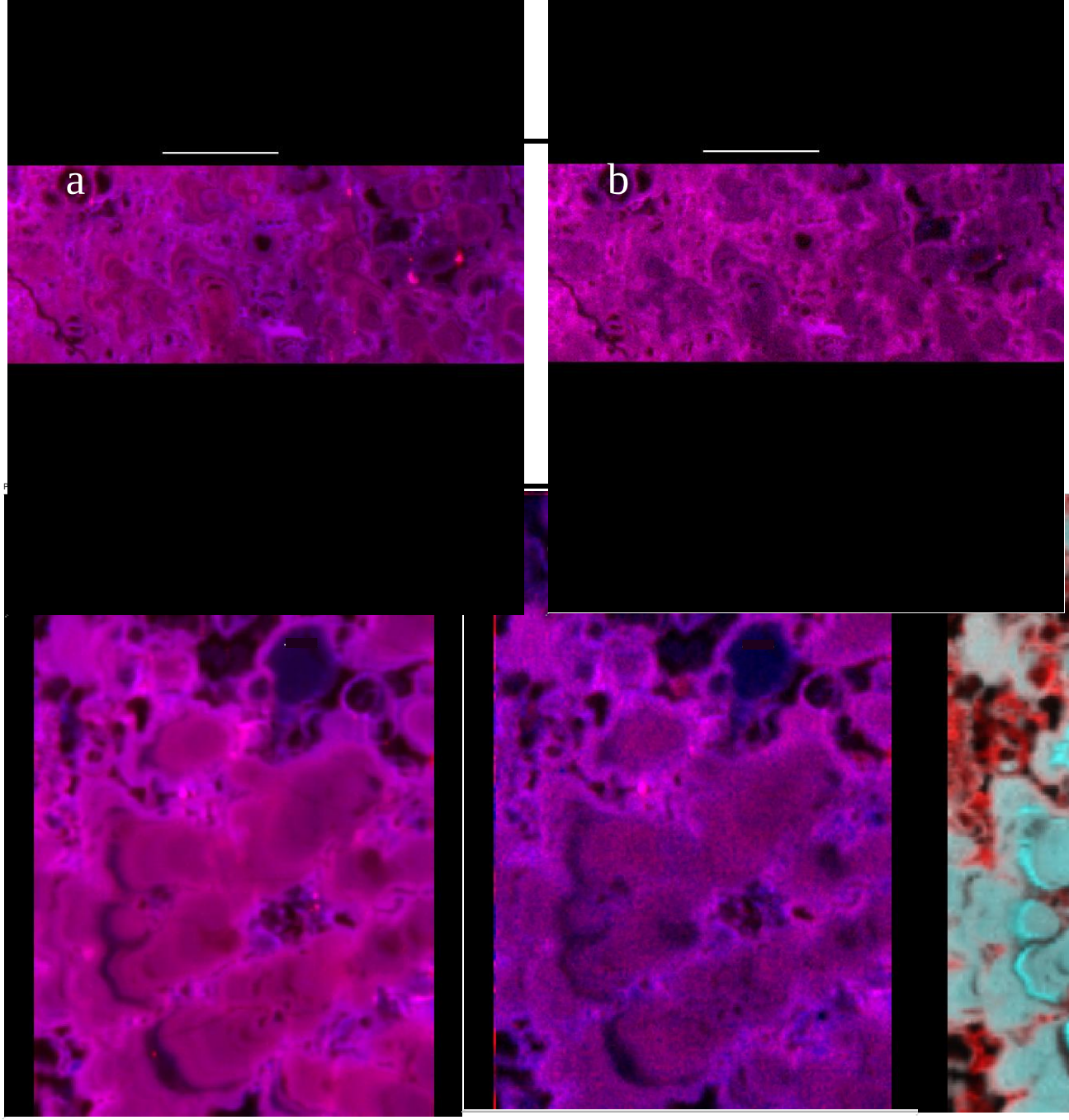
a
b
FeMn

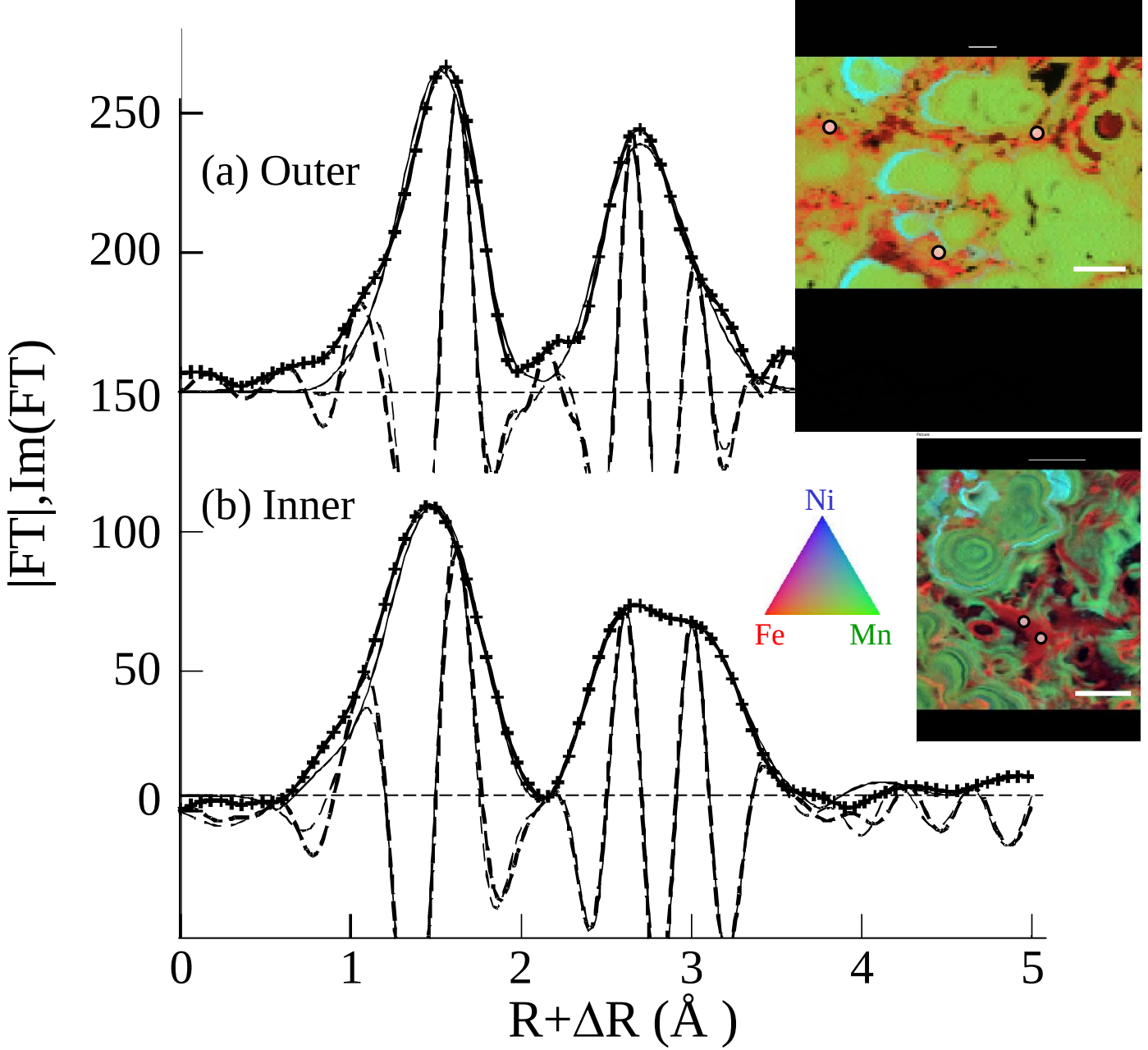
(a) Outer
(b) Inner
250
200
150
100
50
0
|FT|,Im(FT)
0
1
2
3
4
5
R+ΔR (Å)
Ni
Fe
Mn

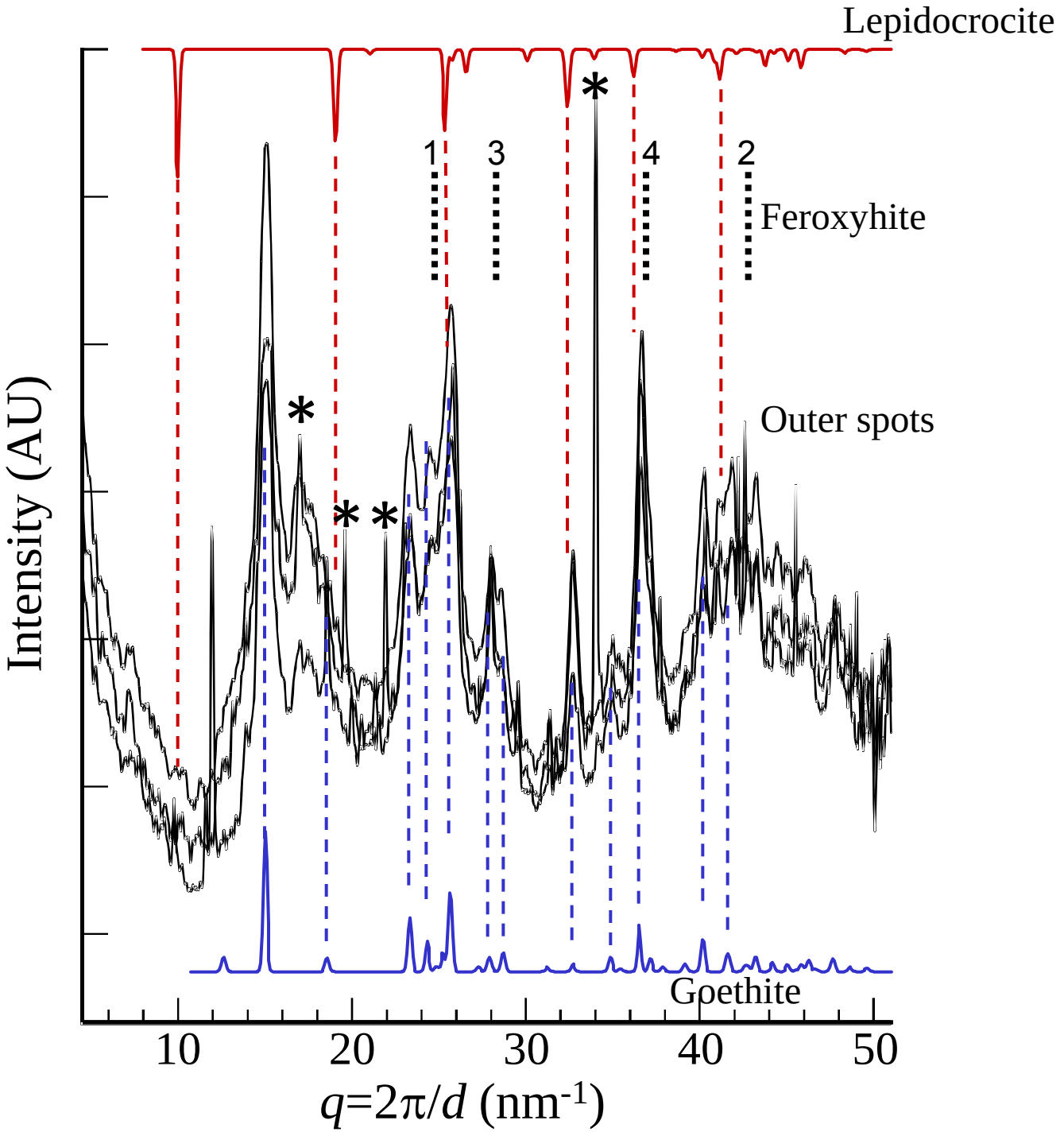
Lepidocrocite
1
3
4
2
Feroxyhite
Outer spots
Goethite
Intensity (AU)
10
20
30
40
50
q=2π/d (nm-1)

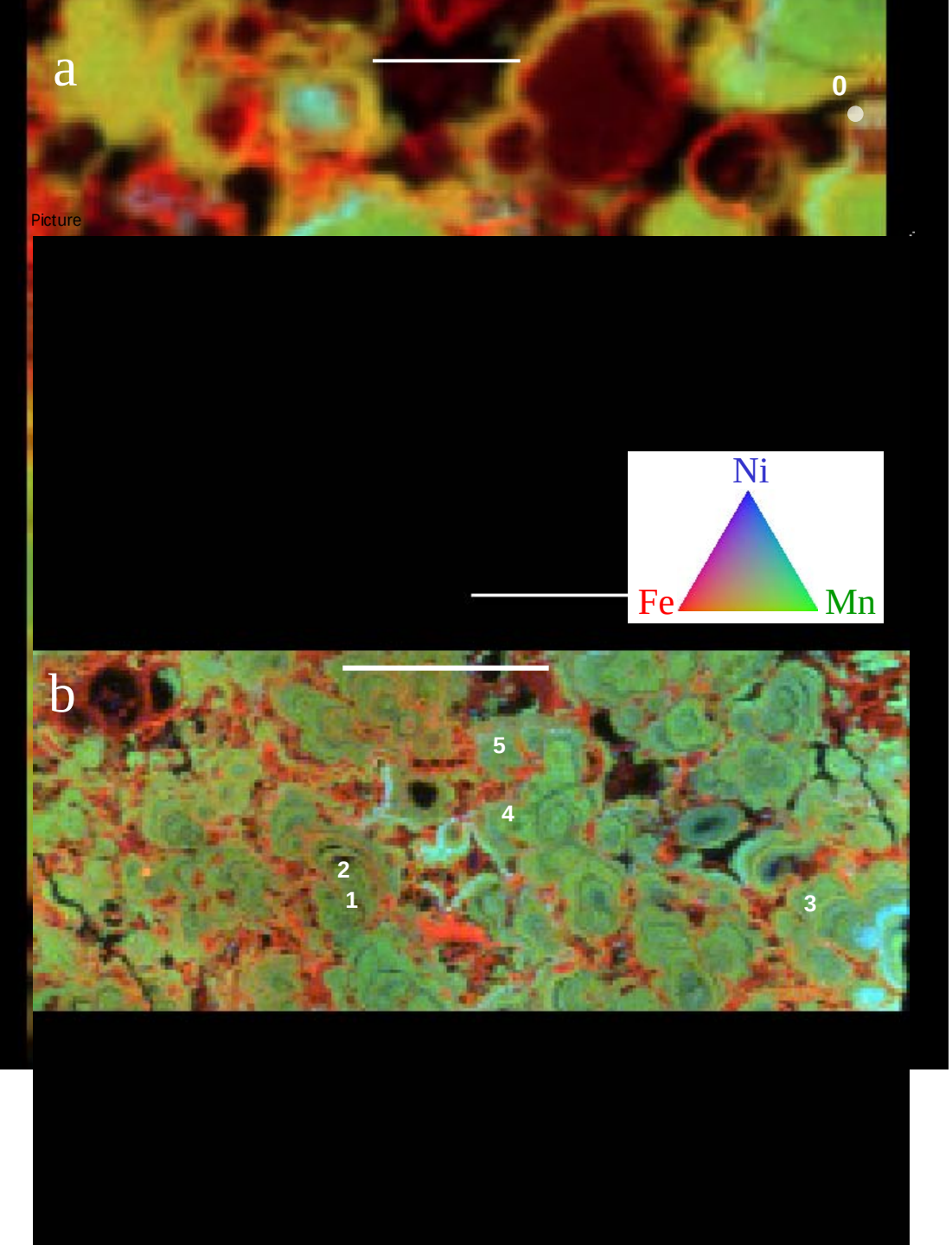
a
0
Picture
Ni
Fe
Mn
b
5
4
2
1
3

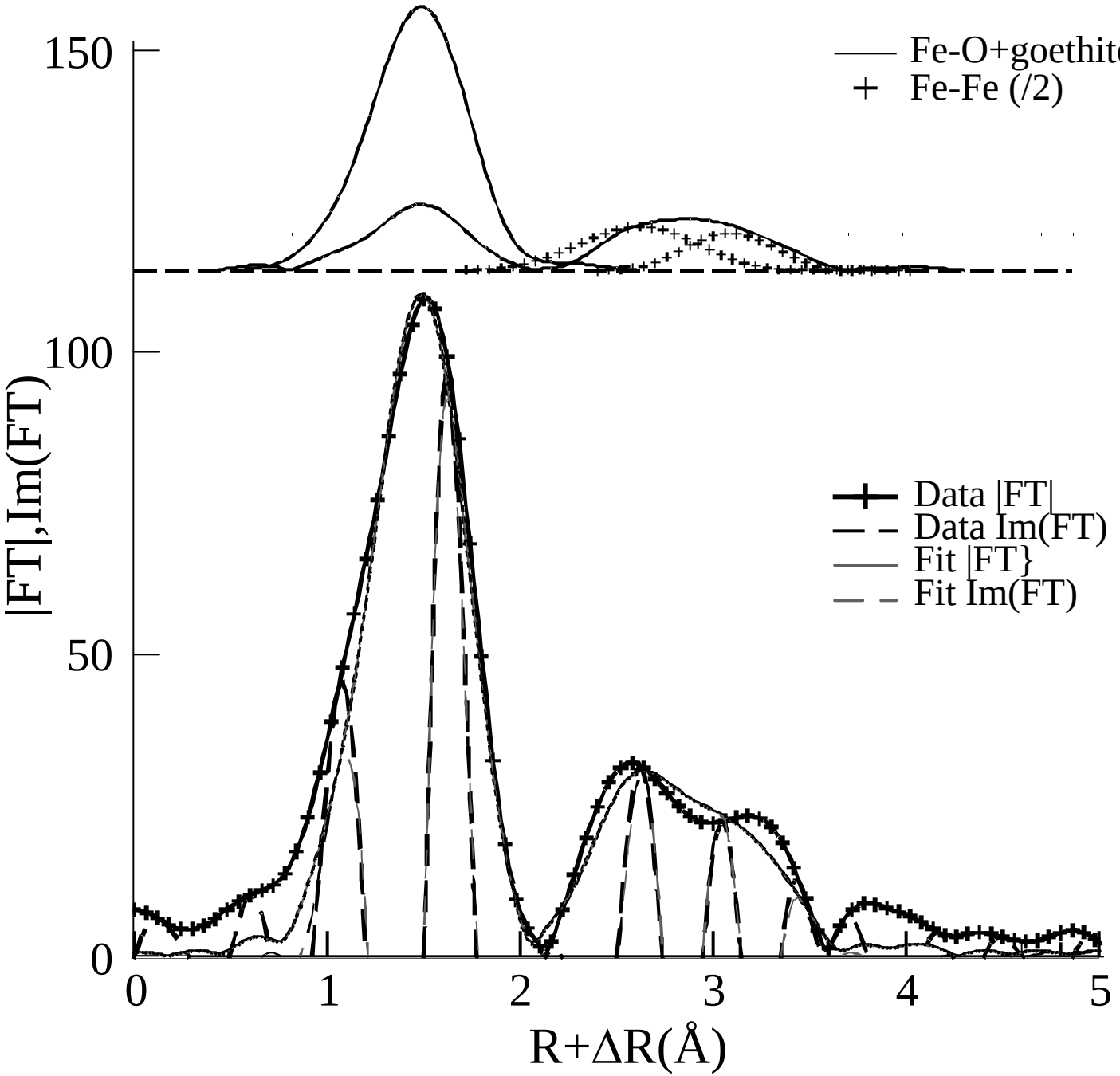
150
100
50
0
|FT|,Im(FT)
0
1
2
3
4
5
R+ΔR(Å)
Fe-O+goethite (/2)
Fe-Fe (/2)
Data |FT|
Data Im(FT)
Fit |FT}
Fit Im(FT)

ACCEPTED MANUSCRIPT

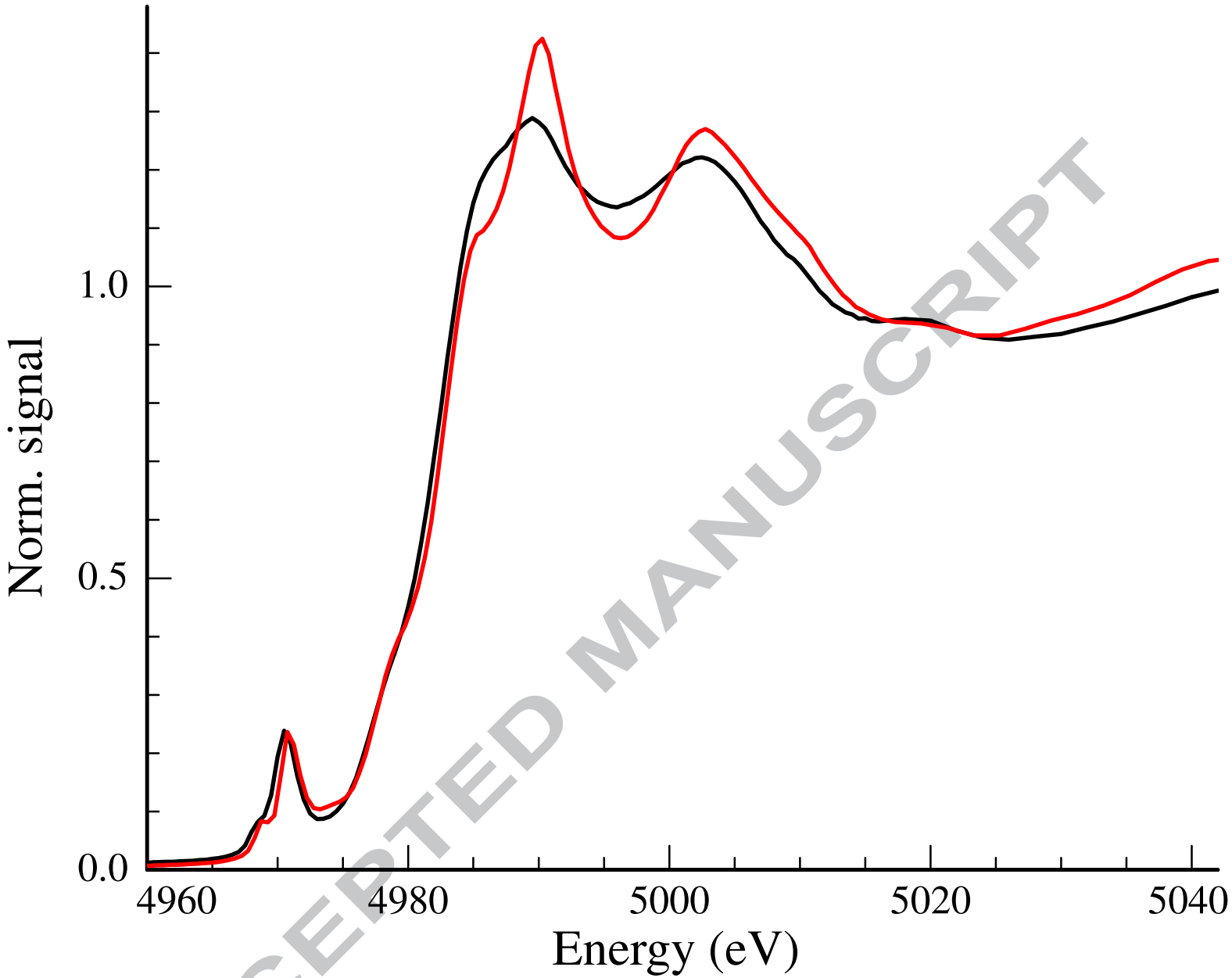

ACCEPTED MANUSCRIPT

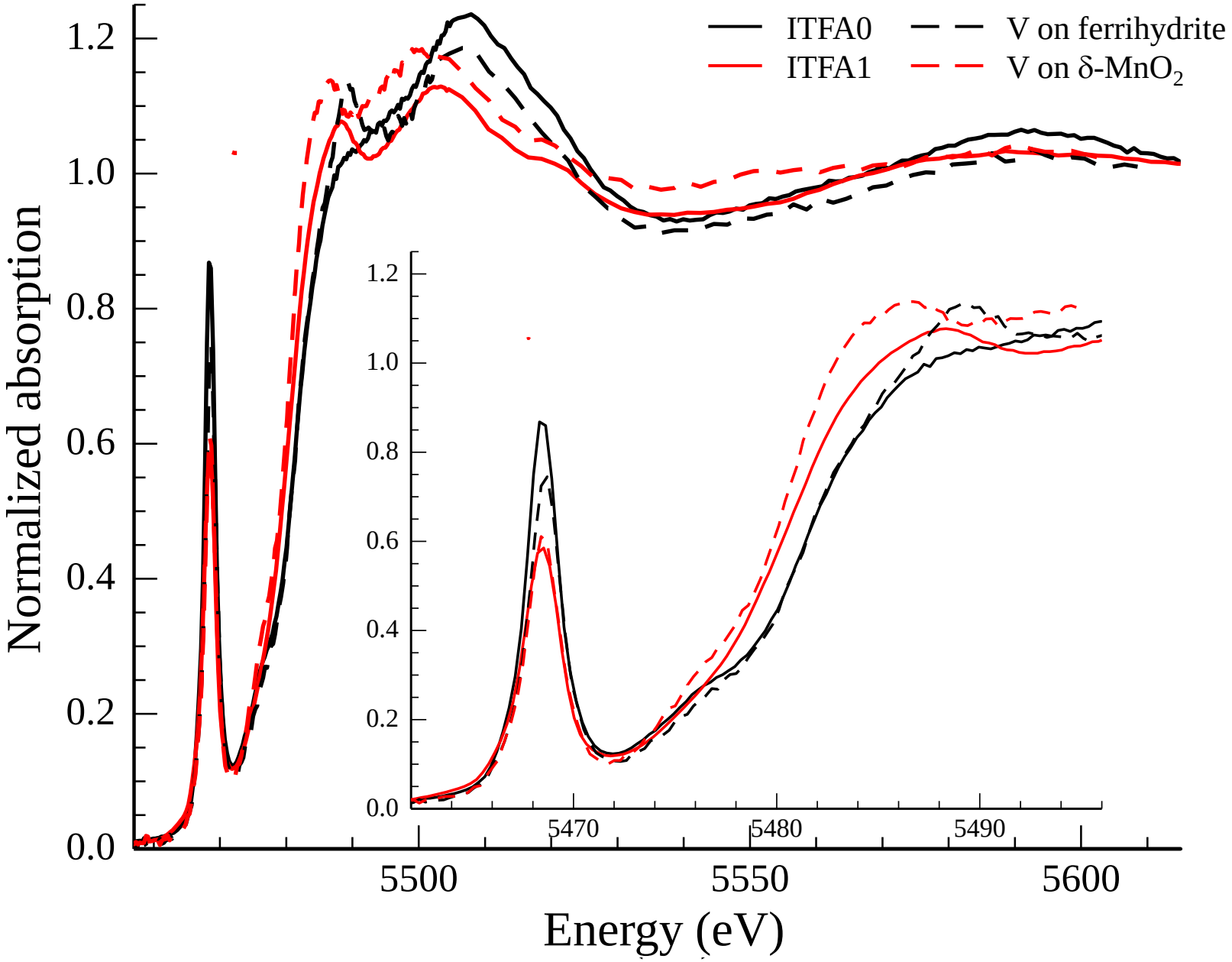
ITFA0
ITFA1
V on ferrihydrite
V on δ-MnO2
Normalized absorption
Energy (eV)
0.0
0.2
0.4
0.6
0.8
1.0
1.2
5500
5550
5600
5470
5480
5490

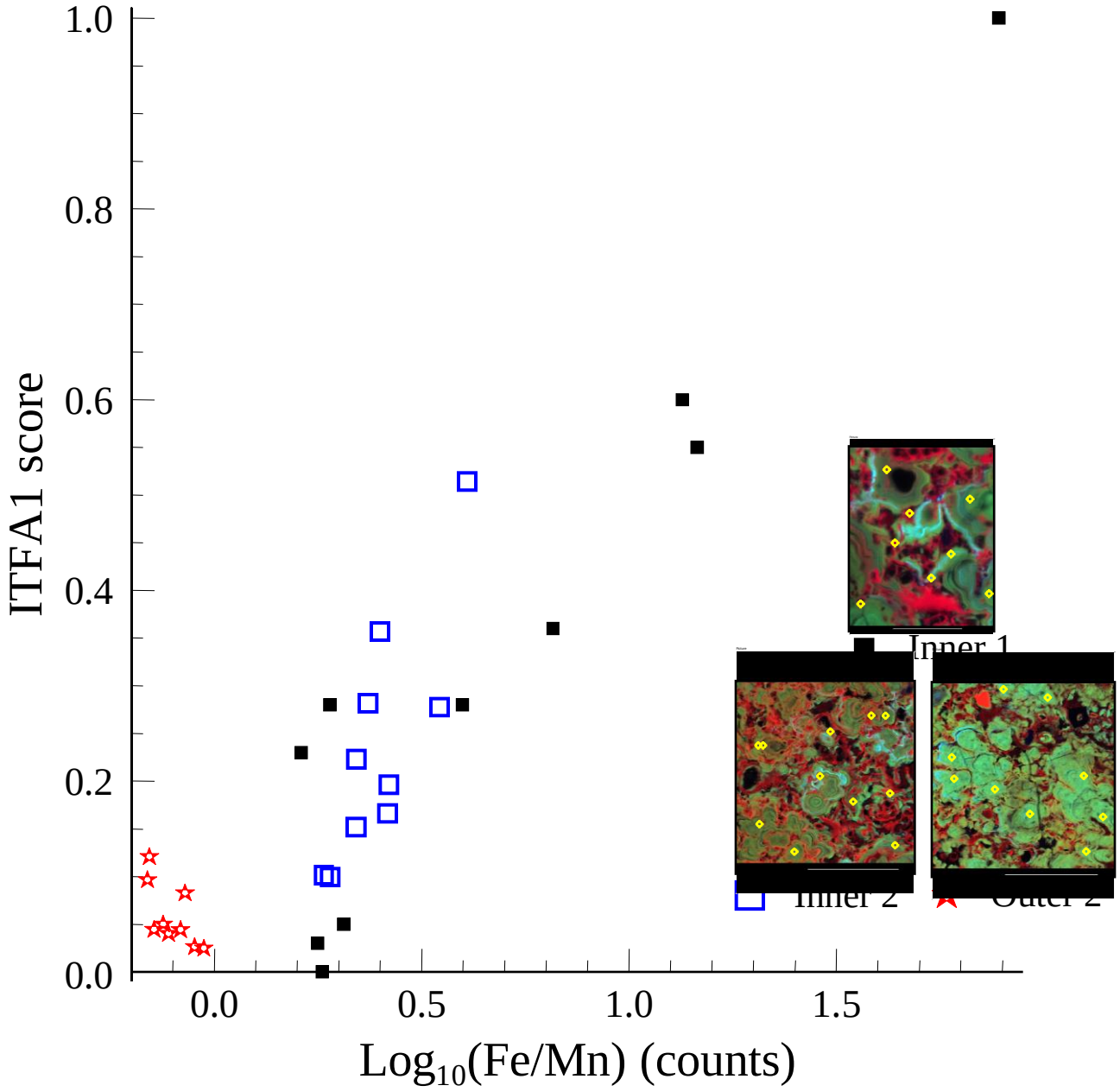
1.0
0.8
0.6
0.4
0.2
0.0
ITFA1 score
0.0
0.5
1.0
1.5
Log10(Fe/Mn) (counts)
Inner 1
Inner 2
Outer 2

ACCEPTED MANUSCRIPT

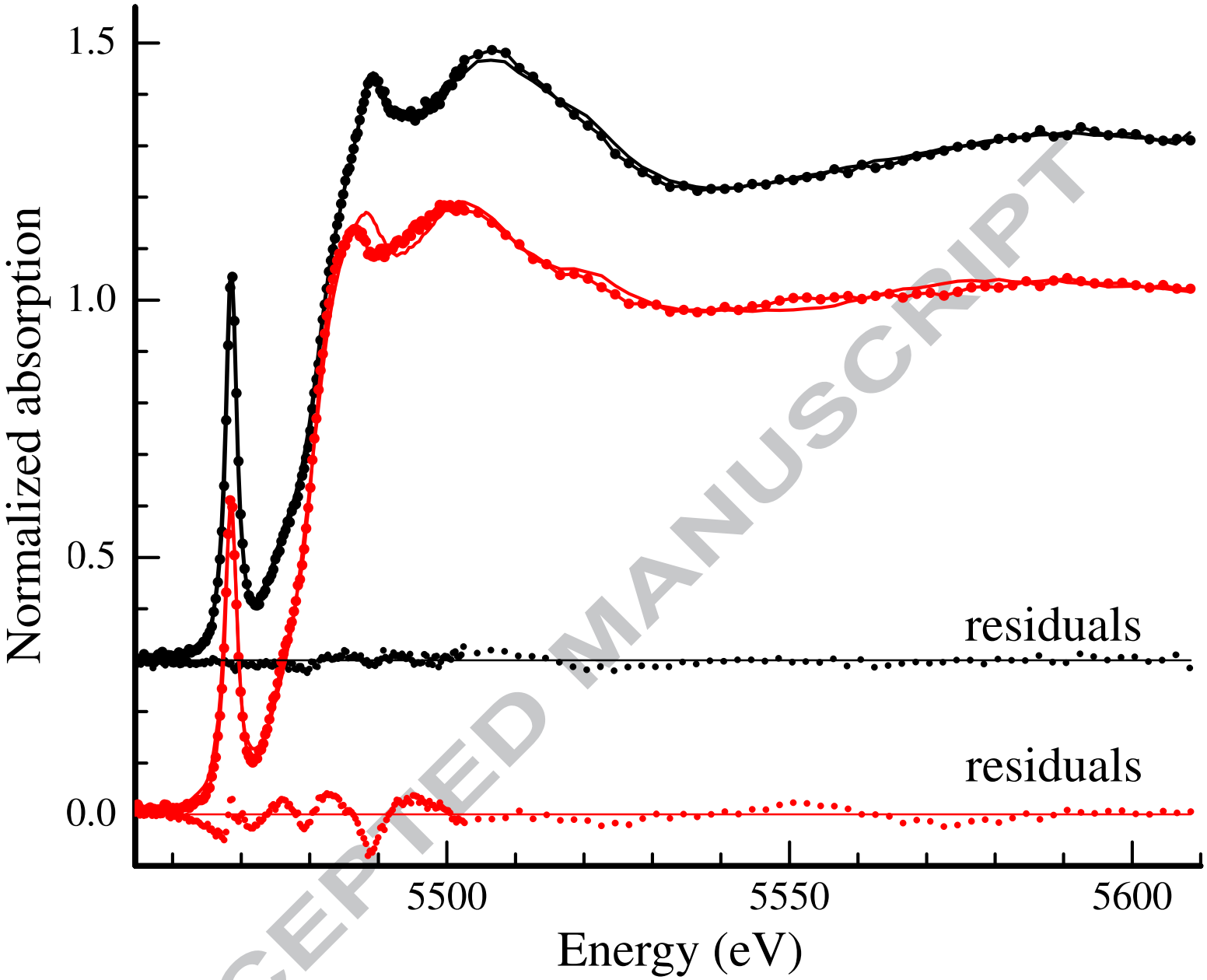

ACCEPTED MANUSCRIPT